UNIVERSITY OF BIRMINGHAM

Modeling of the Dec. 22nd 2018 Anak Krakatau volcano lateral collapse and tsunami based on recent field surveys

Grilli, S.t.; Zhang, C.; Kirby, J.t.; Grilli, A.r.; Tappin, D.r.; Watt, S.f.l.; Hunt, J.e.; Novellino, A.; Engwell, S.; Nurshal, M.e.m.; Abdurrachman, M.; Cassidy, M.; Madden-nadeau, A.l.; Day, S.

Link to publication on Research at Birmingham portal

1 **Modeling of the Dec. 22ⁿᵈ 2018 Anak Krakatau volcano lateral collapse and**

2 **tsunami based on recent field surveys: comparison with observed tsunami**

3 **impact**

4

5 Grilli[1] S.T., Zhang[2] C., Kirby[2] J.T., Grilli[1] A.R., Tappin[3,4] D.R., Watt[5] S.F.L., Hunt[6], J.E.,

6 Novellino[3], A., Engwell[3] S., Nurshal M.E.M.[7], Abdurrachman M.[7], Cassidy, M.[8], Madden-

7 Nadeau A.L.[8] and S. Day[4]

8
9 1. Department of Ocean Engineering, University of Rhode Island, USA

10 2. Center for Applied Coastal Research, University of Delaware, USA

11 3. British Geological Survey, Nottingham, UK

12 4. University College, London, UK

13 5. School of Geography, Earth and Environmental Sciences, University of Birmingham, UK

14 6. National Oceanography Centre, Southampton, UK

15 7. Bandung Institute of Technology, Indonesia

16 8. Department of Earth Sciences, University of Oxford, UK

17

18 **Abstract**

19 The Dec. 22, 2018 lateral collapse of the Anak Krakatau (AK) volcano in the Sunda Straits of

20 Indonesia discharged volcaniclastic material into the 250 m deep caldera southwest of the volcano

21 and generated a large tsunami, causing runups of up to 85 m in the near-field, and 13.5 m in the

22 far-field, on the nearby coasts of Sumatra and Java. The tsunami caused 437 fatalities, the greatest

23 number from a volcanically-induced tsunami since the catastrophic explosive caldera-forming

24 eruption of Krakatau in 1883 and the sector collapse of Ritter Island in 1888. For the first time in

25 over 100 years, the 2018 AK event provides an opportunity to study a major volcanically-generated

26 tsunami that caused widespread loss of life and significant damage. Here, we present numerical

27 simulations of the collapse and tsunami generation, propagation, and coastal impact, with state-of

28 the-art numerical models, using both a new parametrization of the collapse and a near-field

1

29   bathymetric dataset based on our 2019 field surveys and satellite images. These subaerial and

30   submarine data sets are used to constrain the geometry and magnitude of the landslide mechanism,

31   which show that the primary landslide scar bisected the AK edifice, cutting behind the central vent

32   and removing 50% of its subaerial volume. The primary landslide volume is estimated to range

33   from $0.175 - 0.313$ km^3, based on uncertainties in the shape of the submerged part of the failure

34   plane. This is supported by an independent estimate of the primary landslide deposit volume of

35   0.214 ± 0.036 km^3. Given uncertainties in the failure volume, we define a range of potential failure

36   surfaces that span these values in 4 collapse scenarios of volume ranging from 0.175 to 0.313 km^3.

37   These AK collapses are modeled, assuming either a granular or viscous fluid rheology, together

38   with their corresponding tsunami generation and propagation. Observations of a single tsunami,

39   with no subsequent waves, are consistent with our interpretation of landslide failure in a rapid,

40   single phase of movement rather than a more piecemeal process, generating a tsunami which

41   reached nearby coastlines within ~30 minutes. For both modelled rheologies, the 0.224 km^3

42   collapse (second and preferred scenario) most successfully reproduces the near- and far-field

43   tsunami flow depth and runup observed in all post-event field survey results, tide gauge records,

44   and eyewitness reports to date, suggesting our estimated landslide volume range is appropriate.

45   This event highlights the significant hazard posed by relatively small-scale lateral volcanic

46   collapses, which can occur *en-masse*, without any precursory signals, and are an efficient and

47   unpredictable tsunami source. Our successful simulations demonstrate that current numerical

48   models can accurately forecast tsunami hazards from these events. In cases such as Anak

49   Krakatau's, the absence of precursory warning signals, together with the short travel time

50   following tsunami initiation present a major challenge for mitigating tsunami coastal impact,

51   stressing the need to develop and install early warning systems for such events.

53 1 Introduction

54 Over the past 20 years, catastrophic tsunamis in Papua New Guinea (1998), the Indian Ocean

55 (2004), and Japan (2011) have led to major advances in understanding and modeling tsunamis from

56 submarine landslides, earthquakes, and dual mechanisms. These advances have mainly focused on

57 improving constraints on these recent events and their geographical distribution, together with

58 improved numerical tsunami modelling capability (e.g., Tappin et al., 2008; Grilli et al., 2007;

59 Ioualalen et al., 2007; Grilli et al., 2013; Kirby et al., 2013; Tappin et al., 2014; see Yavari-Ramshe

60 and Ataie-Ashtiani, 2016, for a recent review). Tsunamis from volcanic eruptions and collapses

61 remain less well-studied because, up until recently, there were few well-recorded and researched

62 events. However, they have the potential for generating mega-tsunamis (Paris et al., 2020b),

63 resulting in significant loss of life and property (Day, 2015; Paris, 2015), and they account for

64 approximately 20% of all volcanic fatalities over the past 400 years (Auker et al., 2013).

65 Most known lateral collapse events at volcanic islands are prehistoric, and their tsunami

66 generation is inferred from the distribution of their submarine deposits rather than being based on

67 direct observations. In some cases, elevated boulder deposits provide supporting evidence of

68 extreme wave heights being produced by these collapses (e.g., Paris et al., 2020b). Many such

69 events were large-volume (> 10 km^3) lateral volcanic collapses of ocean islands above mantle

70 plumes, such as in the Canary Islands (e.g., Ward and Day, 2001; Day et al., 2005; Løvholt et al.,

71 2008; Abadie et al., 2012; Giachetti et al., 2012) and Hawaii (e.g., McMurty et al., 2003). In

72 contrast, some were smaller scale events on subduction zone volcanoes, including historical edifice

73 collapses such as those at Ritter Island 1888 (5 km^3; Ward and Day, 2003) and Stromboli 2002

74 (0.01 km^3; Tinti et al., 2006; Fornaciai et al., 2019). Of historical events, the best studied eruption-

generated tsunami is that at Krakatau, Indonesia in 1883 (Verbeek, 1983, 1885; Simkin and Fiske, 1983; Siswowidjoyo, 1983). During theis eruption, there were 19 tsunamis, with the most destructive generated during the final, cataclysmic, caldera collapse and the associated emplacement of pyroclastic flow material into the sea, which destroyed the volcanic edifice and caused 33,000 fatalities (Simkin and Fiske, 1983). Another highly destructive volcanic tsunami was generated by the lateral collapse of Ritter Island in 1888. This ~5 km^3 flank collapse is the largest recorded volume lost from an island volcano in a single event in historical times (Ward and Day, 2003; Karstens et al., 2019; Watt et al., 2019). The death toll in the Ritter tsunami is poorly constrained, with the highest estimate being about 3,000 deaths (Johnson, 1987). Due to the paucity of data on most volcanic events, the results of their tsunami modelling have not been fully validated and both landslide source mechanisms (e.g., Hunt et al., 2011; Ward and Day, 2003; Watt et al., 2019) and the generated tsunamis (e.g., Day et al., 2005; Løvholt et al., 2008; Giachetti et al., 2011; Abadie et al., 2012, 2020; Tehranirad et al., 2015; Paris, 2015), remain poorly documented, so are a challenge to model. Any tsunamigenic volcanic collapse thus provides an opportunity to improve our understanding of coupled flank-failure and tsunami-generating processes, and to test and develop current landslide-tsunami numerical models. As the largest volcanic-island lateral collapse since that at Ritter Island in 1888, and with more detailed observations of both the collapse and the generated tsunami, the failure of Anak Krakatau (AK) volcano, Indonesia, in December 2018 provides important new insights that advance our general understanding of volcanic tsunamis. With remarkable prescience, Giachetti et al. (2012) modeled a tsunami from a collapse of the SW flank of the Anak Krakatau volcano, similar to that of Dec. 28th 2018, using a hypothetical 0.28 km^3 volume. The resulting wave heights and arrival times along surrounding coastlines foreshadowed the 2018 event.

98   In the evening of December 22, 2018, at 20:55-57 local time (Walter et al., 2019), following

99   a 6 month period of relatively heightened eruptive activity, a lateral collapse occurred on the

100   southwest flank of the AK volcano in the Sunda Strait, Indonesia (Figs. 1 and S1). The collapse

101   generated a tsunami that impacted the adjacent coastlines of Java and Sumatra within 30 minutes

102   (Grilli et al., 2019), causing up to 13.5 m runups and resulting in 437 fatalities, 13,000 people

103   injured, 33,000 displaced and thousands of buildings destroyed (AHA, 2018; Andersen, 2018;

104   Muhari, 2018, 2019; Grilli et al., 2019; TDMRC, 2019). The AK event was the most damaging

105   volcanically-generated tsunami since the 1883 eruption of Krakatau and the 1888 lateral-collapse

106   of Ritter Island. The numerous observations of AK's 2018 collapse and tsunami, including those

107   previously unpublished by the authors of this paper, provide a unique dataset for both

108   understanding this event and testing state-of-the-art tsunami modelling methodologies against

109   direct observations, with the modelling constrained by both volcanic tsunami source parameters

110   and observations of the generated waves and their coastal impact.

111   Here, we develop volcanic lateral-collapse scenarios based on new data from our 2019

112   subaerial and submarine surveys at AK (Hunt et al., 2021; Priyanto et al., 2021), model both the

113   resulting slides and tsunami generation, and compare the latter with data from near- and far-field

114   surveys of tsunami inundation and runup.. In our approach, the marine geology surveys inform the

115   slide and tsunami simulations, which in turn through comparison with tsunami data help confirm

116   the likeliest collapse scenario.

117   Published subaerial data on the collapse (e.g., Williams et al., 2019; Novellino et al., 2020;

118   Perttu et al., 2020) has provided the basis for previous tsunami modelling (e.g., Grilli et al., 2019).

119   The new numerical modeling presented hereafter is also based on this remote (mainly satellite)

120   subaerial data but also, for the first time, on a hydroacoustic data set of multibeam echosounder

121 (MBES) bathymetry and seismic reflection data acquired to the southwest of the volcano after

122 AK's eruption, in August 2019 (Hunt et al., 2021; Priyanto et al., 2021).

123   An important aspect of our new modelling of the 2018 collapse and tsunami generation is

124 the use of the latest version of the three-dimensional non-hydrostatic model NHWAVE (Zhang et

125 al., 2021a,b). This model features effects of vertical accelerations, not just in the water (as in earlier

126 implementations) but also within the slide material itself. Our earlier modelling of the event had

127 neglected vertical acceleration (i.e., non-hydrostatic) effects within the slide layer (Grilli et al.,

128 2019); this was also the case in other modeling studies of this event that are detailed later. We

129 show that including these effects is important for an accurate simulation of both wave generation

130 from the collapse and the near-field runups. These new simulations are also performed at a much

131 higher resolution, owing in part to the new high-resolution bathymetric and topographic data from

132 our 2019 field survey and its subsequent analyses and reconciliations with the subaerial

133 observations (Hunt et al., 2021). Model results for both the near- and far-field tsunami generation,

134 propagation and coastal impact are validated against time series of sea surface elevation recorded

135 at tide-gauges in the Sunda Straits together with all published field observations and eyewitness

136 accounts to date of onland tsunami flow depth and runup, both on islands in close proximity to AK

137 (including the August 2019 authors' drone survey), and in the far-field on the coasts of Java and

138 Sumatra.

139   The combined subaerial and marine data sets, and results presented here, constrain the style

140 and mechanism of the AK lateral collapse and also test current volcanic landslide-tsunami models,

141 which can be used to predict the behavior of similar events at other volcanic islands. The results,

142 therefore, are an important contribution towards improved assessment of tsunami hazard from

143 analogous events in the future, and also provide an improved basis for developing mitigation

144 strategies for volcanic tsunamis.

145

146 **2 Background and earlier modeling work**

147 *2.1. Geologic and volcanologic context*

148 AK (Fig. 1) is a composite volcanic cone that developed on the northeast margin of the 250 m deep

149 flooded caldera formed by the 1883 eruption of Krakatau (Figs. 2a,3a; Camus et al., 1987; Stehn,

150 1929). It developed from and so is aligned with the feeder vents of the 1883 Krakatau eruption

151 (Verbeek, 1885, 1983). During the past 90 years of frequent eruptive activity, AK has grown from

152 a submarine volcano to a subaerial edifice, emerging in 1929. With a pre-2018 collapse height

153 estimated at about 335 m (Grilli et al., 2019), it formed an island with a diameter of 1.5-2 km. On

154 the SW flank of AK, coastline retreats of several hundred meters in 1934, 1935 and 1949

155 (Neumann van Padang, 1983; Hunt et al., 2021) imply long-lived instability of the edifice on this

156 sector (Hunt et al., 2021). The NW-SE orientation of the retreats align with both the underlying

157 caldera-wall scarp and the 2018 collapse scar (Fig. 2a). The retreats are a result of two related

158 factors: i) AK's location on the NE margin of the 250-m deep 1883 caldera; and ii) the

159 asymmetrical pattern of island growth (see discussion in Hunt et al., 2021). The early submarine

160 activity of AK before and during first emergence of the island in 1929 was dominated by

161 phreatomagmatic explosions (Umbgrove 1928; Stehn 1929). Similar explosions continued after

162 first emergence and built-up a low-angle tuff cone around a vent to which the sea continued to gain

163 access until the 1960s. At that time the vent dried out and further subaerial eruptive activity

164 produced lava flows on the SW side of the island, and Vulcanian and Strombolian explosions that

165 built up a scoria cone around the vent (Siswowidjoyo, 1983). This activity continued into the 21st

166   Century, with numerous small eruptions punctuated by more violent explosive episodes, giving

167   the island its pre-collapse form of steep-sided central pyroclastic cone, with lava deltas extending

168   the island on most sides, except the sheltered NE where the tuff cone rim was at its highest, but

169   especially in the NW and SE (Abdurrachman et al., 2018). During a subaerial eruption in 1981

170   (Camus et al., 1987), a ~2 m high tsunami was recorded on Rakata, a remnant of the 1883 eruption

171   and the southernmost and largest island of the contemporary Krakatau archipelago (Fig. 1), which

172   was inferred to originate from a small flank landslide. The event highlighted the potential

173   instability of the southwest flank of the volcano (Camus et al., 1987) but, apart from this, no other

174   tsunamis from AK have been reported.

175   The recent period of AK volcanic activity started in June 2018 and continued into

176   December (https://volcano.si.edu/volcano.cfm?vn=262000), producing Strombolian explosions,

177   lava flows, and ash plumes reaching altitudes of up to 5 km (Anon, 2018; Fig. 2 in Paris et al.,

178   2020a; Figs. S1c,d; Hunt et al.'s 2021 supplementary material). On Dec. 22, 2018, a major lateral

179   collapse occurred on AK's southwest flank which discharged volcaniclastic material into the sea

180   and triggered a destructive tsunami (Andersen, 2018; PVMBG, 2018). Based on seismic records

181   (Gurney, 2018), eyewitness reports (e.g., Andersen, 2018; Perttu et al., 2020), and the agreement

182   of modelled waves with tsunami arrival times at tide gauges (Ina-COAP, 2019; see below; Fig. 1a,

183   Table 3), Grilli et al. (2019) estimated that the collapse took place at 20:55′–57′ (UTC + 7), a time

184   range later confirmed and used by other authors of numerical models (e.g., Borrero et al., 2020;

185   Mulia et al., 2020; Paris et al., 2020a; Zengaffinen et al., 2010), and confirmed in the interpretation

186   of seismic signals by Walter et al. (2019), who timed the collapse at 20:55′. Within 30 minutes of

187   the collapse a tsunami flooded the coasts of west Java and southeast Sumatra, causing up to 13.5

188   m on-land runups. The tsunami struck near high tide (+1.5 m above the vertical datum on average

189   at four tide gauge in Java and Sumatra; Fig. 1a), which increased its impact (AHA, 2018; Muhari,

190   2018, 2019; Grilli et al., 2019; TDMRC, 2019).

191

192   *2.2. Previous modeling of the 2018 AK event*

193   In light of the modelling published by Giachetti et al. (2012), Grilli et al. (2019) performed

194   the first comprehensive numerical simulations of the Dec. 22nd 2018 AK collapse, based on

195   satellite observations on the days following the event, drone and field surveys of near-field tsunami

196   impact conducted in early January 2019 (Reynolds, 2019; TDMRC, 2019; Fig. S1), and historical

197   data on the growth of AK (see, e.g., Hunt et al., 2021). The modelling of AK's flank collapse and

198   tsunami generation was based on a range of failure surfaces with corresponding collapse volumes

199   of 0.22-0.30 km^3 and used the three-dimensional (3D) non-hydrostatic (NH) model NHWAVE

200   (Ma et al., 2012, 2015; Kirby et al., 2016), in which the collapse was represented by a depth-

201   integrated (hydrostatic) layer of a granular material or dense viscous fluid. From the modelling it

202   was proposed that a 0.27 km^3 collapse volume produced the modelled tsunami that best reproduced

203   the near- and far-field tsunami propagation and impact, with the far-field modeling using the fully

204   nonlinear and dispersive Boussinesq model FUNWAVE (Shi et al., 2012). In these simulations a

205   90 or 100 m Cartesian grid was used in each model, respectively, with 5 vertical layers in the 3D

206   NHWAVE grid.

207   Numerical simulations of the 2018 AK collapse and tsunami post-dating Grilli et al. (2019),

208   detailed in the following paragraphs, were also based on hypothetical source parameters derived

209   from a variety of, mainly indirect, data. In these studies, the various assumed/hypothetical failure

210   surfaces gave collapse volumes in the range $\approx$ 0.14-0.33 km^3, which were both smaller and larger

211   than the 0.27 km^3 of Grilli et al.'s (2019). In Ye et al.'s (2020) study, inversion of broadband

212   seismic data was used to infer a collapse volume of ≈ 0.20 km^3. In some studies, an empirical

213   analytical or experimental (from laboratory tests) landslide source was specified directly on the

214   free surface without an actual modeling of the source (e.g., Heidarzadeh et al., 2020a; Borrero et

215   al., 2020). In other modeling studies, new interpretations of subaerial observations were used (see

216   Hunt et al., 2021 for a discussion) and the flank collapse and tsunami generation modeled for a

217   variety of volumes and geometries (e.g., Mulia et al., 2020; Ren et al., 2020; Omira and Ramalho,

218   2020; Paris et al., 2020a; Zengaffinen et al., 2020; Dogan et al., 2021). In the latter models, tsunami

219   generation was based on various rheologies (granular, viscoplastic, Bingham) and simulated using

220   a two-dimensional (2D) two-layer model.   There were also important differences in tsunami

221   propagation models used in these various studies, with some using a dispersive model (e.g., Mulia

222   et al., 2020; Paris et al., 2020a; Borrero et al., 2020) and others using a non-dispersive tsunami

223   propagation model (e.g., Heidarzadeh et al., 2020a; Ren et al., 2020; Omira and Ramalho, 2020;

224   Dogan et al., 2021). As landslide tsunamis are typically made of shorter, more dispersive, wave

225   trains, they often require the use of a dispersive long wave model for their accurate modeling (e.g.,

226   Ma et al., 2012; Glimsdal et al., 2013; Tappin et al., 2014; Grilli et al. 2015, 2017; Schambach et

227   al., 2019). For the 2018 AK event, Paris et al. (2020a) concluded that dispersive effects were

228   important during tsunami generation and propagation, whereas Zengaffinen et al. (2020) found

229   that they were not large in the shallow water areas of the Sunda Straits (as would have been

230   expected), to the north and south of AK. More specifically:

231   • In one of the more comprehensive recent studies, Zengaffinen et al. (2020) modeled the

232   tsunami using the rate of mass release, the landslide volume, the material yield strength, and

233   orientation of the landslide failure plane, together with the 2D two-layer depth-averaged

234   coupled model BingClaw, to identify different failure mechanisms, landslide evolution, and

235   tsunami generation. The depth-integrated landslide layer was based on a viscoplastic flow

236   rheology, coupled with depth-averaged long wave and shallow water type models to simulate

237   tsunami propagation. With a volume of 0.28 km^3, identical to that of Giachetti et al. (2012),

238   the numerical simulations provided a reasonable match to the observed tsunami surface

239   elevation amplitudes and inundation heights in the far-field. Overall the results were consistent

240   with those of Grilli et al.'s (2019) preferred 0.27 km^3 scenario, and discrepancies between the

241   simulated and observed arrival times at the offshore gauges were attributed to the (poor)

242   accuracy of the available bathymetry, rather than to their model. To match these, to the north

243   of Krakatau, Zengaffinen et al. (2020) arbitrarily increased the water depths in this area.

244   • Paris et al. (2020a) used the 2D two-layer depth-averaged coupled model AVALANCHE,

245   which features a granular rheology and a Coulomb friction for the slide description, with

246   dispersive effects for the water flow part. From pre- and post-collapse satellite and aerial

247   images, and a satisfactory comparison of the simulated water waves with far-field observations

248   (tide gauges and field surveys), they reconstructed a total (subaerial and submarine) landslide

249   volume of 0.15 km^3, at the lower end of the volume range in the various studies described here.

250   • Ren et al. (2020) applied a 2D two-layer depth-averaged coupled non-dispersive model

251   throughout, with the slide layer modeled as a dense fluid. Using two nested grids, the smaller

252   having a 30 m resolution and the larger a coarse 230 m resolution, and 0.1-0.3 km^3 collapse

253   scenarios, they showed a reasonable agreement with the first wave at the far-field tide gauges.

254   • Mulia et al. (2020) integrated the landslide thickness over the estimated source area and,

255   assuming a failure surface similar to that of Giachetti et al. (2012), except for a slightly steeper

256   slope, obtained a collapse volume of 0.24 km^3 (slightly smaller than that of Giachetti et al.,

257   2012, and Grilli et al., 2019). Using the 2D two-layer depth-averaged coupled model VolcFlow

258   to simulate avalanche dynamics (here assuming a constant retarding stress throughout), and

259   FUNWAVE for the far-field tsunami, their landslide generated higher than 40 m waves in the

260   vicinity of the volcano. As with other studies the tsunami attenuated rapidly as it propagated

261   away from the generation area, resulting in lower than 2 m wave heights at tide gauges around

262   the Sunda Strait.

263 • Omira and Ramalho (2020) used a multi-layer viscoplastic model to simulate the collapse, with

264   a 2D slide layer based on a Bingham rheology and an upper water layer in which the (non-

265   dispersive) Nonlinear Shallow Water Equations are solved. They simulated a sequence of two

266   failures (5 s apart) of 0.1 and 0.035 km^3, respectively, and computed both the near- and far-

267   field tsunami propagation using the same model. They used high-resolution bathy/topo data

268   (see Table 1) to create a 10 m DEM, but it is unclear what their model resolution was. The

269   collapse generated a 45 m leading wave near the volcano, which caused up to 60 m runup on

270   nearby islands. Although they obtain a reasonable agreement at the 4 tide gauges for the leading

271   wave, they indicate strong tsunami dissipation in the far-field, only computing maximum

272   runups of 4 m in Java. This could result from their non-dispersive model and/or excessive

273   numerical dissipation and use of a coarse grid in the simulations.

274 • Finally, in the latest study to date, Dogan et al. (2021) modeled a 0.25 km^3 collapse (based on

275   a maximum elevation for AK of only 260 m, smaller than used in other studies) and its tsunami

276   generation, using Imamura and Imteaz (1995)'s two-layer long wave model. Tsunami

277   propagation to the far-field was then simulated using the non-dispersive NSW model NAMI

278   DANCE, in an 80 m resolution grid. Little details are given of the parameterization of their

279   dense fluid rheology in the slide model or the rationale for defining the pre- and post-failure

280   volcano geometry, including the selected failure surface. However, they show a good

281 agreement with both arrival times and elevation time series measured at the 4 tide gages in

282 Java and Sumatra. Based on observed bathymetric changes in pre- and post-event surveys, they

283 model tsunami generation from additional submarine slope failures on the north and south

284 sides of the caldera, but conclude that these did not contribute to and hence were not

285 simultaneous with AK's 2018 event.

286 The main characteristics of the previous modeling studies discussed above are listed in Table 1.

287 All of these studies used different AK collapse scenarios and a wide spectrum of

288 approaches and tsunami modelling, but the differences in tsunami elevations predicted at the far-

289 field tide gages were small; there were larger differences in predicted far-field runups, but some

290 of these could be explained by differences in grid resolution and model physics. While details of

291 a tsunami source become less important when the distance from the source increases, here, the

292 small differences in the predicted far-field tsunami impact between various modeling studies were

293 in great part because the landslide mechanisms were based on inverse methodologies and, hence,

294 were partly or wholly hypothetical. So, although the recorded far-field tsunami was reproduced, it

295 was not based on the actual collapse mechanism but, at best, on direct evidence such as from

296 satellite imagery, or indirect evidence such as from seismic observations of the subaerial collapse.

297 In all studies, hydroacoustic data such as multibeam bathymetry or seismic reflection data, to

298 confirm the submarine components of the landslide source mechanism, was lacking. In the

299 modelling studies using a semi-empirical landslide source (e.g., Borrero et al., 2020; Heidarzadeh

300 et al., 2020a), the collapse volume and hence source strength were adjusted based on field

301 observations of the tsunami (e.g., near- and/or far-field runup and tide gauges). The validation was

302 then from the forward numerical modeling of the tsunami, which is rather circular. Other modeling

303 studies using an actual slide mechanism also adjusted or confirmed their collapse scenario and

304 volume, to achieve a good agreement of tsunami simulations with far-field data.

305   While making some source adjustments to best match the far-field tsunami observations,

306 most previous studies also demonstrated a moderate sensitivity of the predicted far-field tsunami

307 impact to the landslide source characteristics. This shows that far-field tsunami observations alone

308 cannot fully constrain the 2018 AK collapse parameters and, hence, stresses the need for also using

309 near-field tsunami data and, more importantly, marine surveys to do so, as will be done in this

310 work.

311

312 **3 Methods**

313 3.1 *Study area, computational grids, and bathymetric/topographic data*

314 Figure 1a shows the entire study area and the footprint of the two computational grids used in the

315 simulations of: (grid G2) AK's collapse and tsunami generation/near-field impact, using the 3D

316 model NHWAVE; and (grid G1) tsunami propagation and far-field impact, using the 2D model

317 FUNWAVE, together with their bathymetric and topographic data.

318   The near-field Grid G2 is defined with a $\Delta x = \Delta y = 30$ m horizontal resolution (Table 2),

319 from the composite bathymetry developed by Hunt et al. (2021), based on the new multibeam

320 echosounding (MBES) bathymetry acquired during their August 2019 field surveys (Figs. 2a,b),

321 combined with: (i) unpublished Sparker seismic reflection profiles acquired in 2017; (ii) basin

322 bathymetry from Deplus et al. (1995) manually modified within the deep part of the caldera to add

323 up to 10 m of sediment infill between 1995 and 2018 (based on interpreted seismic profiles in Hunt

324 et al., 2021); (iii) an 8 m DEM for the islands of the Krakatau archipelago (from

14

325 http://tides.big.go.id/DEMNAS); and (iv) topography from Gouhier and Paris (2018) for AK itself,

326 based on the DEMNAS DEM, with modifications to account for island growth in 2018.

327   The far-field grid G1 (Fig. 1a; Table 2) is Cartesian with a 50 m resolution and its

328 bathymetric and topographic data is interpolated from Giachetti et al. (2012)'s 100 m resolution

329 dataset, which was developed outside of Krakatau's caldera based on GEBCO data. The GEBCO

330 data is referred to mean sea level (MSL); GEBCO, however, indicates that in some shallow water

331 areas, their dataset includes data from sources having a vertical datum other than MSL. Note that

332 even though the bathymetric data is coarser than the model grid, using a finer model grid allows

333 for a more accurate resolution of the nearshore wave physics. Our model grid is also finer than the

334 90 m resolution used by Grilli et al. (2019).

335   Regarding the reference mean water level (MWL), Grilli et al. (2019) indicated that, when

336 the tsunami was generated, the average elevation at the four tide gauges (WG 6-9; Fig. 1a; Table

337 3) was approximately +1.5 m over the vertical datum. Because of this, simulations were based on

338 adding 1.5 m to the bathymetric data (i.e.using water depths of MWL = MSL + 1.5 m, where it is

339 assumed that the bathymetric datum is mean sea level (MSL). However, as noted above, there may

340 be inconsistency in the vertical datum used in the bathymetric compilation. Moreover, both at the

341 time and still at present, the reference datum for the tide gauges is unknown, but in the absence of

342 other constraints we assumed a common vertical datum for our bathymetric datasets and the tide

343 gauges. Given the local tidal range, the elevation at the time of the tsunami was more likely

344 between 0.5 and 1.0 m above the true MSL (see discussion in the Supplementary file #S3). To

345 assess the effect of the uncertainty in both nearshore bathymetry and in the tide gauge datum value

346 with respect to the MSL, we performed a sensitivity study of model results to the assumed MWL

347 (for the likeliest collapse scenario defined in the next section; see Supplementary file #S3 and

15

348   Table 5). This demonstrates that, within the range MSL +0.5 to + 2 m, model results were little

349   affected by the water-depth adjustment, with each of the MWL values giving results that compared

350   similarly well to the field data. Hence, for consistency and comparison with our earlier modeling

351   work (Grilli et al., 2019), we selected the same MWL = MSL + 1.5 m in this study.. This value

352   was added to the interpolated bathymetric data for both Grid G1 and G2, prior to performing

353   tsunami simulations. When comparing simulation results to field data referenced to MSL or some

354   other datum, a relevant correction was made to the field data.

355   3.2 *Landslide source model*

356   The landslide source model was defined on the pre-collapse bathymetry/topography grid G2

357   defined above, using constraints that drew on the post-collapse bathymetric survey of Hunt et al.

358   (2021), particularly to define the boundaries of the submarine failure surface, as well as an updated

359   interpretation of the subaerial failure plane. The latter was based on a sequence of Synthetic-

360   Aperture Radar (SAR) satellite images collected in the days following the collapse, alongside

361   aerial imagery collected on Dec. 23rd 2018. These images proved particularly important in defining

362   the northern and southern bounds of the subaerial collapse scar, since their position could be

363   precisely defined based on the complex coastal shape of the lava deltas. The COSMO-SkyMed

364   SAR imagery from Dec. 23rd 2018 confirms the shape of the failure scar between these two coastal

365   points (cf. Hunt et al., 2021) and was used to pick both the upper line of the headwall and the point

366   where this intersected sea-level (i.e. the 0-m contour; e.g., Figs. 2c,d). These two boundaries were

367   used to define the subaerial dimensions of the modeled landslide failure plane, and we thus

368   consider this component of the failure surface to be fixed in the range of source models described

369   below.

370   To address the limitations of the published tsunami source models of the collapse

371   mechanism and the landslide resulting from the 2018 AK flank collapse, as mentioned before,

372   MBES bathymetry and seismic data were acquired in the 250 m deep basin on the southwest flank

373   of the volcano in August 2019 (Hunt et al., 2021). From detailed analyses of this marine survey

374   data (Figs. 2a,b) these authors mapped the submarine landslide resulting from the volcanic collapse

375   and estimated the landslide outrun deposit volume at 0.214 ± 0.036 km^3. Rather than being

376   extensively disintegrated, the submarine deposit is mainly composed of large intact blocks (Figs.

377   2a,b), confirming that the event occurred as a single *en masse* slide with limited fragmentation,

378   rather than in a more piecemeal, multi-staged process. This mechanism is also confirmed by

379   seismic data (Gurney, 2018). From these characteristics, while there were many large landslide

380   blocks in the deposits (up to hundreds of meters across), a granular slide rheology was deemed

381   more relevant in our subsequent modeling than a dense fluid rheology, which is more appropriate

382   for debris flows (although both were simulated for completeness). An additional unit, to the

383   southwest of this main deposit, with a volume of 0.022 ± 0.006 km^3, was interpreted as a secondary

384   sediment failure (i.e., debris flow), resulting from sediment mobilized by the primary landslide

385   emplacement and seafloor incision (Hunt et al., 2021).

386   A range of volumes were defined for the 2018 AK collapse, based on the marine survey in

387   combination with new analyses of subaerial observations from high-resolution satellite imagery,

388   and aerial photography. This estimated a subaerial collapse volume of 0.098 ± 0.019 km^3 (cf. Hunt

389   et al., 2021). Beneath sea level, the lateral margins of the collapse scar were defined using

390   bathymetric features on the submerged flank of AK, evident on the post-collapse marine survey.

391   A subtle step in the submerged SW flank, at -100 to -120 m described by Hunt et al. (2021), that

392   may correspond to the base of the failure plane, was used to define the minimum collapse volume

393   scenario (Figs. 2c,d), which has a shallower failure surface than that of Grilli et al. (2019) for their

394   minimum 0.22 km^3 volume scenario. Using the features identified by Hunt et al. (2021), the

395   boundary of the submarine failure plane was estimated as a broadly elliptical form, and this

396   boundary was then projected onto our pre-collapse bathymetric grid. This was used to define a

397   smooth concave failure plane, constrained by the gradient of the subaerial scar and the requirement

398   to cut the vent position beneath sea-level, defining a minimum collapse volume of 0.175 km^3.

399   Precise identification of the shape and margins of the failure surface is still uncertain because of

400   burial by post-collapse deposits. Additional features on the NW and S flank of AK, that align with

401   the subaerial margins of the scar, alongside deeper features on the SW flank (cf. Hunt et al., 2021),

402   may also relate to the collapse plane and were used by Hunt et al. (2021) to define a possible larger,

403   deeper-seated failure surface. Using the same approach as described above, the failure volume in

404   this largest possible scenario was estimated at 0.313 km^3 (Figs. 2c,d). Both end-point collapse

405   volumes include the 0.098 km^3 subaerial component.

406   Comparing the deposit volume, estimated purely from the MBES and seismic reflection

407   survey, to the failure volumes estimated based on the inferred failure surface and geometry, we

408   find good consistency. The main part of the landslide deposits form a blocky mass, identified in

409   the August 2019 MBES data (modeled a,b) and interpreted as representing material directly derived

410   from the island flanks, with a volume of 0.214 ± 0.036 km^3. The estimated primary deposit volume

411   of 0.214 km^3 lies between the two end-point failure-surface-derived volumes described above

412   (Figs. 2c,d). Given that the failed mass is likely to have expanded upon fragmentation, and is

413   potentially bulked via seafloor erosion, an increase in the volume of the landslide deposit,

414   compared to the volume derived from the shallowest estimated failure surface, could potentially

415   be accounted for by these phenomena. A further uncertainty arises from the possibility that some

416   of the failed mass could have remained within the scar region and been subsequently buried

417   (although there is no evidence to suggest that this volume is significant), and would not be included

418   in the estimate of deposit volume derived from marine geophysical data. Consequently, although

419   quite unlikely, we cannot entirely reject a scenario with a deeper-seated failure plane and a larger

420   source volume, up to a maximum of 0.313 km^3, although our interpretation is that the primary

421   failure volume was likely closer to our minimum estimate (0.175 km^3).

422   Within the blocky landslide deposit (Figs. 2a,b), it can be assumed that transport of all

423   material derived from the volcano flanks was tsunamigenic. There is potential for expansion and

424   incorporation of seafloor material during slide motion, and we thus use the scar-derived volumes

425   rather than the deposit volume to define the range of source-volumes for tsunami modelling. In

426   addition to this, mobilization of seafloor sediment triggered by primary landslide emplacement

427   (forming the secondary debris flow deposit) may also have contributed to tsunami generation.

428   However, given that this must have followed the main stage of landslide motion, was in relatively

429   deeper water, and was an order of magnitude smaller in volume, we assume that this material was

430   not significant in contributing to the main tsunami generation. The 0.022 ± 0.006 km^3 debris flow

431   volume also falls well within the range of uncertainties of the estimated landslide volume.

432   In the modeling, the above uncertainty in AK's collapse parameters is represented by

433   defining four landslide (and failure surface) geometries and corresponding volume scenarios, for

434   which we use the same subaerial pre-collapse geometry in every case (based on the SAR-derived

435   collapse-scar position), intersecting the NE flank at about 100 m elevation (Fig. 2d). For the

436   submarine surface, we use the minimum and maximum bounds of the failure surface described by

437   Hunt et al. (2021) and discussed above, projecting the positions of the defined collapse margins

438   onto our pre-collapse model grid. Alongside this, we define two intermediate scenarios. The four

439   scenarios have a maximum depth on the SW flank ranging from -80 to -220 m (Fig. 2d) and their

440   failure surfaces all cut the active vent position at depths ranging from 25 to 40 m, which is

441   consistent with the vigorous Surtseyan eruptive activity that immediately followed the collapse

442   (Hunt et al., 2021). Using the pre-collapse AK topography (maximum 335 m), refined based on

443   high-resolution satellite images (Novellino et al., 2020) and the assumed concave failure surfaces,

444   the volumes associated with the four scenarios were computed to: (1) 0.313; (2) 0.272; (3) 0.224;

445   and (4) 0.175 km^3. The latter two compare closely with the deposit volume estimate, given

446   uncertainties and allowing for some degree of expansion and/or bulking by erosion, while the first

447   two scenarios are larger, but consistent with some bathymetric features and the possibility that

448   some of the failure mass remained within the collapse scar. The first scenario is close to the largest

449   volume originally simulated by Grilli et al. (2019), and the second is close to what they concluded

450   to be the likeliest scenario.

451   Among these scenarios, the third one, with a 0.224 km^3 volume, is deemed the likeliest

452   volume scenario in the modeling, in terms of providing the best representation of the tsunamigenic

453   mass movement consistent with the marine geophysical data. Given that there remain uncertainties

454   in the precise form of the failure plane, the mean deposit volume of 0.214 km^3 from Hunt et al.

455   (2021) is the best representation of the tsunamigenic mass (even if we cannot constrain the extent

456   of expansion and bulking) and, the 0.224 km^3 volume also allows for the possibility of some

457   tsunamigenic contribution from the associated secondary debris flow. The post-collapse

458   bathymetry for the likeliest scenario (0.224 km^3) is shown in Figs. 1c and 3b. Note that the latter

459   figure shows that, as expected, the specified failure surfaces are not planar but slightly concave.

460   This is a necessary shape given the relatively steep gradient (30-40 degrees) of the subaerial failure

461   plane (constrained from SAR imagery and consistent with the volcanic vent being cut beneath sea-

462   level) but the need for the foot of the failure to emerge within the submerged flank of AK, and is

463   also a failure-surface shape typical of the morphology of volcanic lateral collapses.

464

465   3.3 *Tsunami generation and propagation simulations*

466   3.3.1 *Numerical tsunami models.*

467   Two numerical models are used in simulations of AK's 2018 collapse and tsunami

468   generation, propagation and coastal impact, which are briefly described below.

469   NHWAVE (Ma et al., 2012), a three-dimensional (3D) non-hydrostatic model, is used to

470   simulate both AK's volcanic collapse scenarios, and the corresponding tsunami generation and

471   near-field impact, on AK and surrounding caldera islands, in Grid G2 with a 30 m horizontal

472   Cartesian grid with 1,155 by 9,55 cells, using 7 boundary fitted water layers in a vertical σ-

473   coordinate system (Figs. 1b,c; Table 2). With one layer, the model provides the same order of

474   dispersion as a Boussinesq model such as FUNWAVE, detailed hereafter, and higher-order

475   dispersion effects when using more layers. NHWAVE has been used, and experimentally validated

476   (e.g., Ma et al., 2012), to model tsunami generation from solid slides (landslides or slumps) (e.g.,

477   Grilli et al., 2015; Schambach et al., 2019) and from dual sources coseismic/solid submarine mass

478   failures (Tappin et al., 2014). NHWAVE was extended to simulate tsunami generation by

479   deforming slides, both submarine and subaerial, assumed to behave as either a granular medium

480   or a dense Newtonian fluid (Ma et al., 2015; Kirby et al., 2016). These NHWAVE models were

481   applied to case studies for deforming slide sources (e.g., Grilli et al., 2017b, 2019; Schambach et

482   al., 2019), and validated based on laboratory experiments for those studies (Grilli et al., 2017b), as

483   well as for dual sources involving a combination of coseismic and deforming underwater/subaerial

484   slides (e.g., Grilli et al., 2019; Schambach et al., 2020a,b).

485   Since the work of Grilli et al. (2019), a new version of NHWAVE has been developed

486   (Zhang et al., 2021a,b) that includes effects of vertical acceleration (i.e., non-hydrostatic pressures)

487   within the slide material layer, which was neglected in the earlier implementation (Ma et al., 2015).

488   Considering the steep slopes of both AK and the surrounding islands, it was anticipated that such

489   effects might be important. This was confirmed here by comparing, in Supplementary file #2,

490   simulations of the Grilli et al. (2019) preferred volume scenario (0.272 km^3), with both granular

491   and viscous rheologies, and with and without the non-hydrostatic effects included in the equations

492   for the slide layers. Results for both rheologies showed that slide motion and wave generation are

493   significantly affected, with larger waves generated and much larger runups occurring on the near-

494   field islands, particularly Panjang and Sertung, when non-hydrostatic effects are neglected. When

495   comparing with near-field runup measured in field surveys, a much better agreement was obtained

496   with the newer version of the model that accounts for non-hydrostatic effects within the slide layer.

497   For these reasons, this newer version of NHWAVE by Zhang et al. (2021a,b) was used in the

498   present study.

499   FUNWAVE-TVD (Shi et al., 2012; version 3.0 is used), a two-dimensional (2D) fully

500   nonlinear Boussinesq wave model, is used to simulate far-field tsunami propagation and coastal

501   impact in Cartesian Grid G1 with a 50 m resolution and 3,900 by 3,680 cells (Fig. 1a; Table 2); a

502   Cartesian rather than a spherical grid is acceptable in view of the small geographic area considered

503   here. To improve dispersive properties, the horizontal velocity used in this Boussinesq model is

504   that at a depth $z = -0.531\ h$. To prevent reflections from the open boundaries of grid G1 (Fig. 1a),

505   10.8 km (or 216 grid cells) wide sponge layers are specified along its 4 boundaries.

506   Both NHWAVE and FUNWAVE-TVD used a Courant number and Froude cap condition

507   to adaptively specify the time step in simulations to achieve optimal accuracy. In shallow water

508   and during runup this can lead to using prohibitively small time steps, which is prevented here by

509   specifying a minimum depth truncation of 1 m and 0.05 m in the NHWAVE and FUNWAVE

510   simulations, respectively. The 0.05 m minimum depth has little effect on FUNWAVE simulations

511   of the far-field tsunami impact. In the near-field, considering the very large waves and runups

512   modeled with NHWAVE, the 1 m minimum depth also does not significantly affect simulation

513   results. Both models are parallelized with MPI, allowing efficient implementation on large

514   computer clusters. Here we typically used 20 processors to run each scenario. Finally, both models

515   are open source and available on *github*, together with their user manual and benchmarking

516   examples.

517   3.3.2 *Modeling methodology.*

518   Simulations of AK's collapse and tsunami generation and near-field impact are first performed in

519   grid G2 with NHWAVE, for the 4 volume scenarios, and for each of those, assuming either a

520   granular or a dense fluid rheology (Table 4). When the slide is fully at rest and waves approach

521   the boundary of grid G1 (Fig. 1a), NHWAVE results for surface elevation and horizontal velocity

522   interpolated at 0.531 times the local depth are used to initialize FUNWAVE simulations in Grid

523   G1. These are then run for another 2 hours of tsunami propagation time, to make sure all the

524   diffraction, and multiple reflection effects on the tsunami from the shores and many islands of the

525   Sunda Straits are included in the results.

526   In NHWAVE simulations, for each of the four specified collapse surfaces and volumes

527   (Figs. 2c,d), we use the same parameterization of the slide rheology as in Grilli et al. (2019), i.e.:

528   (i) a Newtonian fluid of density ρ_c = 1,550 kg/m^3 and the kinematic viscosity of a debris flow, ν_c

529   = 0.5 m^2/s; or (ii) a granular medium with ρ_c = 1,900 kg/m^3 for the solid part and, similar to

530   Giachetti et al. (2012), an internal friction angle ϕ_{ic} = 10°, a basal friction angle ϕ_{bc} = 2°, and a 40%

531 porosity. With this data, assuming a water density ρ_w = 1,025 kg/m³, the average density of the

532 granular medium is ρ_{ac} = 1,550 kg/m³ (Table 5). For each of these 8 scenarios, NHWAVE was run

533 up to 420 s; however, results showed that the time when the generated tsunami waves approach

534 the boundary of grid G1 is t = 380 s (e.g., Fig. 7h), which is used to prevent any perturbation of

535 the solution.

536   Finally, in both model grids, in the absence of site-specific data we specify a constant

537 bottom friction coefficient C_d = 0.0025, which corresponds to coarse sand. While this value may

538 be too small to model friction on the rough walls of the 250 m deep caldera to the SW of AK,

539 earlier work has shown that bottom friction only significantly affects tsunami propagation

540 (reducing tsunami elevations) over shallow areas where propagation distances represent many

541 dominant wavelengths (Tehranirad et al., 2015). In this case, the bottom velocity caused by the

542 long tsunami waves (in terms of wavelength to depth ratio) is consistently large. Considering the

543 fairly short dominant period of the generated waves, here, bottom friction will only significantly

544 affect tsunami propagation towards Java and Sumatra, in the shallow eastern side of the Sunda

545 Straits. In the caldera to the SW of AK, however, both the water depth is large and the tsunami

546 propagation distances are short, and bottom friction effects are thus expected to be small; hence,

547 the accuracy of the selected C_d value is not important.

548

549 3.4 *Tsunami field survey data*

550 To validate our numerical model results, we used a comprehensive set of data, including marine

551 field surveys, satellite images, bathymetric data as discussed above, and onshore surveys of

552 tsunami impact (Figs. 12-16). The onshore survey data included: (i) the tree line drone survey

553 conducted on Rakata, Sertung and Panjang during our August 2019 field campaign (Figs. 11, 13),

554 and (ii) the runup and flow depth measurements made in the near- and far-field by TDMRC (2019),

555 Muhari et al. (2019), Putra et al. (2020), Borrero et al. (2020), and Heidarzadeh et al. (2020b). In

556 addition, we used the extensive video made by Reynolds (2019), during his 01/11/2019 near-field

557 drone survey of AK and the three surrounding islands, of which salient images were extracted by

558 Grilli et al. (2019) (see their supplementary Fig. S8). One example is in Fig. S1f. These surveys

559 show that, in the near-field, the tsunami generated by AK's 2018 collapse caused up to 85 m runups

560 on the islands of Rakata and Sertung and, in the far-field, up to 13.5 m runups on the nearby coasts

561 of Java and Sumatra.

562   Additionally, as in Grilli et al. (2019) and all other modeling studies, time series of surface

563 elevations simulated for each scenario are compared with detided free surface elevations measured

564 at 4 tide gauges located at (Fig. 1a; Table 3): (5) Serang, Marina Jambu, (6) Ciwandan, (8) Kota-

565 Angung, and (9) Panjang. Grilli et al.'s (2019) Supplementary file #3 explains how the raw data,

566 measured at a 1 minute interval, was detided to obtain the tsunami signal (their Fig. S5) and shows

567 where each tide gauge was located (their Fig. S4), pointing out that each gauge is surrounded by

568 some reflective (or dissipative) coastal structures, not represented in the model grids, that can affect

569 tsunami signal in various ways (including seiching). Table 3 provides the location of each tide

570 gauge, its depth in grid G1 and the arrival time of both a 1 cm tsunami elevation and the first

571 significant wave crest. Fig. 10 shows the complete (detided) tsunami time series measured at each

572 gauge by two different independent instruments operating at each gauge (see details in Grilli et al.,

573 2019); there are some differences (sometimes large) between the measurements of the two

574 instruments at each gauge, which allows quantifying experimental errors. The individual data

575 points in the time series illustrate the coarse 1 minute temporal resolution of the measured signal.

576

4 Tsunami simulation results

4.1 *Slide motion and deposits*

Results of combined NHWAVE-FUNWAVE simulations in Grids G2 and G1 of the 4 volume scenarios ((1) 0.313; (2) 0.272; (3) 0.224; and (4) 0.175 km^3), each with either a granular or viscous rheology (scenarios 1-8 in Table 4), are discussed hereafter.

Figures 4 and 5 show examples of slide motion and free surface elevations simulated with NHWAVE. Fig. 4 first compares results in a vertical plane along a SW transect into AK, for the likeliest volume scenario (0.224 km^3), using either a granular or viscous rheology. We see that the change in rheology only moderately affects slide deformation for small times ($t < 80$ s), and hence corresponding wave generation, but that differences in slide runout are much larger later in time ($t \geq 120$ s), although this stage of motion is no longer tsunamigenic as the slide deposits are too deep. At $t = 200$ s (Fig. 4h) the granular slide deposits have nearly stopped and have mostly accumulated in the caldera, reaching up to a 94 m thickness at the toe of AK's failure surface, whereas the viscous slide deposits have moved further onto the caldera bottom and are still moving. While the granular slide deposits appear to be located in the general area where the actual deposits were mapped during the August 2019 marine survey (Figs. 2b,c) (Hunt et al., 2021), the viscous slide deposits have moved beyond this area; hence simulations based on the granular rheology appear to be more consistent with field data than those with the viscous rheology. This is confirmed in Fig. 5, which shows greater details of the 3D granular slide motion and deposits for the same volume scenario. Here in the last panel at $t = 420$ s (Fig. 5h), we see more clearly where the main slide deposits are located (i.e., their runout) and how thick they are (up to 94 m) at the end of the motion, which is consistent with observations of slide deposits from the marine geophysical survey (Hunt et al., 2021) (compare Fig. 5h with Fig. 2a). In view of the modeled slide idealization by a

600 continuous granular medium, our results for both the slide deposit location and thickness appear

601 to be quite reasonable. It should be noted that while the main collapse deposits are to the SW, the

602 simulation produces a layer of a few meters of granular material deposited on the opposite, NE

603 side of AK and to the NW and SE, which caused small additional wave generation in those

604 directions that however did not affect far-field results which was dominated by larger waves caused

605 by the main collapse. Given the low degrees of fragmentation evident from the very large blocks

606 in the observed deposit (Fig. 2b), these features in model results may not be representative of an

607 actual deposit distribution and are more likely an artifact of a landslide model based on a

608 continuous granular rheology. A similar discrepancy between observed and modeled deposits was

609 noted by Ward and Day (2006) in their study of the 1980 Mount St Helens event, which caused a

610 large debris avalanche.

611 Videos of computed slide motions with and without surface elevation, and for a granular

612 material or a viscous slide are given in supplementary material for the likeliest volume scenario

613 ($0.224\ km^3$); see, AK_slide3D_gran.mp4, AK_ slide3D_visc.mp4, AK_wave_slide3D_gran.mp4,

614 AK_wave_slide3D_visc.mp4.

615

616 4.2 *Near-field tsunami generation*

617 Figures 4 and 7 show snapshots of free surface elevation at times $t = 10, 20, 40, 80, 120,$

618 160, 200, and 380 s, computed for the likeliest volume scenario and a granular or viscous rheology,

619 and Fig. 6 compares time series of surface elevation computed at the 5 numerical wave gauges

620 (Fig. 1b; Table 3) specified in grid G2, for the 8 modeled scenarios (4 volumes and 2 rheologies,

621 scenarios 1-8 in Table 4). Other snapshots of surface elevations for scenarios not shown here look

622   qualitatively similar to those in Fig. 7. Videos of computed surface elevations are given in the

623   supplementary materials.

624   Results in Figs. 4 and 7 show that, in the first 20 s of AK's collapse, a large-scale subaerial

625   slide motion occurs down the volcano, triggering a 50+ m horseshoe-shaped leading elevation

626   wave. From 20-80 s, as the slide moves mostly underwater (for all 4 volume scenarios), an up to

627   30+ m trough (negative elevation wave) forms near the volcano on the SW side, while the leading

628   elevation wave radiates as a cylindrical crest of decreasing height. Figure 6a shows that these

629   processes are well captured at WG 1, which is located directly SW of AK (Fig. 1b; Table 3); at

630   this site, depending on the scenario, a 25-33 m leading elevation wave arrives at $t \approx 60$ s, followed

631   by a 0-10 m trough. At WG 2 and 3, further NW and SW of the volcano, Figs. 6b,c show that, later

632   in time ($t \approx 175$ s), the large elevation wave and its trough (first depression wave) have essentially

633   propagated radially, with only a small decrease in the crest height. The propagation of the

634   horseshoe-shaped leading elevation and first depression waves, with their gradual directional

635   spreading and reduction in elevation, are clearly seen in Figs. 7c to 7h. As these waves propagate

636   away from AK, however, for $t > 80$ s (Fig. 7d), they start interacting with and running up both the

637   N shore of Rakata and S shore of Sertung, causing very large runups.

638   To the NE of AK, for $t > 100$ s, we see a significant tsunami impact occurring on Panjang's

639   southern tip (25+ m runup) and, for $t > 150$ s, a more moderate impact on its northern tip, that are

640   due to both the propagation and refraction around AK's bathymetry of the leading horseshoe-

641   shaped wave (Figs. 7d-f) and later on its reflection off Rakata and Sertung. Finally, in Figs. 7g,h,

642   we see that large waves are propagating in the SW, E and N directions away from AK. For the

643   latter two directions, these waves are well captured at WG 4 and 5 (Figs. 6d,e), where we see

644   leading elevation waves of about 4 and 5 m, respectively. Fig. 7h also confirms that at 380 s, the

645   leading waves have not yet reached and interacted with the outer boundary of Grid G2.

646   Considering the 8 different scenarios, results at WG 1 to 5 in Fig. 6 show that while, overall,

647   all generated waves exhibit the same large-scale characteristics, both a change in collapse volume

648   and rheology affect wave elevation and phase to various extents. Between rheologies, the granular

649   rheology generates slightly smaller leading waves in all cases than the viscous rheology

650   (particularly to the SW), and the larger the collapse volume the larger the wave elevations. [Note

651   that the first conclusion is opposite to that of Grilli et al. (2019) who found that larger waves were

652   generated by a granular slide; this could result from the use here of a much higher grid resolution

653   and the new non-hydrostatic slide model.] At all wave gauges (WG 1-5), the larger leading wave

654   is followed by smaller waves of period as low as T = 30-50 s. Over the 250 m deep caldera, these

655   waves are fully or significantly dispersive. Waves in this period range would be dispersive for

656   depths $h < gT^2/400$ = 3.5-9.8 m, hence for most of their propagation to shore, which justifies using

657   a dispersive long wave model such as FUNWAVE to model AK's collapse far-field tsunami

658   propagation.

659   Fig. 8 shows the envelope of maximum surface elevation computed with NHWAVE in

660   Grid G2 for the likeliest volume scenario (0.224 km^3) and a granular rheology; envelopes for the

661   other scenarios look qualitatively similar and are not shown for the sake of brevity. The figure

662   confirms the large wave generation SW of AK, and shows that large 50-100+ m runups occur on

663   the exposed shores of Rakata and Sertung, and 25 m runup on the south shores of Panjang. These

664   results will be detailed later and compared to field measurements.

665

666   4.3 *Far-field wave propagation and coastal impact on Java and Sumatra*

667   For each of the 8 scenarios, FUNWAVE simulations were initialized with results of NHWAVE in

668   Grid G2 at 380 s (Fig. 7h), interpolated onto Grid G1, and tsunami propagation and coastal impact

669   were simulated up to $t = 7{,}580$ s from the start of the event. Figures 9a-c show snapshots of surface

670   elevation computed with FUNWAVE for the likeliest volume scenario (0.224 km^3) and granular

671   rheology at $t = 380$, 1800 and 3600 s. Results for the other scenarios are qualitatively similar. After

672   30 minutes, Fig. 9b shows that leading tsunami waves have started impacting the SW coast of

673   Java, around the Kolijaah and Panaitan Island areas (Fig. 1a), are impacting the south facing coast

674   of Sebesi (Fig. 1a), and are about to impact the coastlines at Ujung Kulon and Serang, Marina

675   Jambu (tide gauge (WG) 5; Fig. 1a and Table 3). To the north of the grid, leading waves are also

676   impacting the SE tip of Sumatra; waves are also propagating in the direction of tide gauges (WG)

677   6-9 (Fig. 1a; Table 3). After 1 hour of tsunami propagation, Fig. 9c shows a complex pattern of

678   waves in the Sunda Straits, as a result of diffraction-refraction around islands and reflection off

679   the coasts, which justifies performing simulations for a long enough time to capture maximum

680   runup at all locations within Grid G1.

681   Fig. 9d shows the envelope of maximum surface elevation computed with FUNWAVE in

682   Grid G1, after 7,580 s of simulations, for the likeliest (granular) scenario. AK's collapse generated

683   initial waves with a strong SW directionality and a secondary E and N directionality (Fig. 7h),

684   which translates upon far-field propagation into a maximum impact on the SW coast Java and a

685   relatively smaller impact eastward and northward on the coasts of Java and southern Sumatra (see

686   also Fig. 9b). Additionally, wave propagation is affected by a significant bathymetric feature, the

687   moderately steep S-N oriented (around Lon. E. 105.3) linear scarp that divides the shallow eastern

688   half of Sunda Straits from the much deeper Semangka Trough to the west (Fig. 1a). As can be seen

689   in Fig. 9b (and in the animation of model results provided in supplementary material), this

690   bathymetric feature causes a wave guiding effect that reinforces waves to the south onto Panaitan

691   Island, where some of the largest flow depths and runups were measured, and also guides some

692   waves to propagate northward. Comparing bathymetric contours with the maximum envelope in

693   Fig. 9d, we see that little tsunami energy propagated west of Lon. E. 105.3, and that bathymetric

694   focusing also occurs towards Ujung Kulon (Fig. 1a), which is another area where very large runups

695   were measured (see later for details of runups).

696   Surface elevation time series were simulated for the 8 scenarios, combining the four

697   volumes and two rheologies, at the locations of the 4 tide gauges (6-9 in Fig. 1a; Table 3), which

698   are compared to the measured detided surface elevations in Fig. 10. Unlike in the near-field, only

699   small differences (including on arrival time) can be seen here between surface elevations simulated

700   for the 8 different scenarios, indicating that the predictions of the tsunami far-field and impact are

701   less sensitive to details of the collapse scenario assumed for AK (i.e., changes in volume

702   size/geometry and rheology). This was already pointed out by other authors in their discussion of

703   model results (e.g., Heidarzadeh et al., 2020a; Borrero et al., 2020), and also explains why studies

704   that assumed an approximate empirical source for AK's collapse or only a 2D two-layer slide

705   model, with source parameters adjusted to match far-field data at the tide gauges and/or elsewhere,

706   performed reasonably well for predicting coastal impact. However, for future hypothetical

707   collapses, in the total absence of field data to calibrate these models, they might not have fared as

708   well in predicting tsunami impact, from a single forward model simulation.

709   Comparing numerical simulations to tide gauge data, Fig. 10 shows, overall, a good

710   agreement for any scenario, particularly earlier in the time series and more so for WG 6-8 (Figs.

711   10a-c). As summarized in Table 3, arrival times of the leading crest at each gauge are predicted to

712   within 15–78 s of observations. Considering the 1 minute data sampling interval of the gauges,

713   this is an acceptable discrepancy. Later in each tide gauge time series, the phase difference between

714   simulations and observations increases, but the trough-to-crest height of the largest waves are well

715   predicted in the simulations. As previously indicated, later in time, the signal at the tide gauges

716   was increasingly affected by local effects and seiching not resolved and simulated in Grid G1, both

717   due to the limited 50 m resolution and the moderately coarse 100 m resolution of the available

718   nearshore bathymetry and topography. Finally, as reported by eyewitnesses, simulations predict

719   that multiple large waves of fairly short period (2–10 minute) impacted the coast, with the second

720   or later waves being the largest.

721   For each of the 8 scenarios, arrival time at the tide gauges is, to the first-order, governed

722   by wave celerity, which strongly depends on bathymetry and to some extent on frequency for

723   dispersive waves. An additional effect of amplitude dispersion may speed-up wave propagation

724   for the largest waves in the near-field, but this effect will also be similar for all scenarios, as their

725   near-field waves are quite similar (see Fig. 6). This explains the small range in arrival time

726   difference, with the field data listed in Table 3 for the 8 scenarios.

727

728   4.4 *Near-field runups*

729   Grilli et al. (2019) pointed out the intense and continuous phreatomagmatic explosive activity that

730   immediately followed the collapse of AK, both obscuring the skies and discharging large volumes

731   of material that rapidly modified the post-collapse topography of AK and surrounding bathymetry.

732   Hunt et al. (2021) made a detailed analysis of these early stages of AK's post-collapse regrowth,

733   using both satellite images and submarine surveys, and quantified the large changes that took place

734   in AK's coastline and subaerial geometry (e.g., such as Fig. S1b and S1e for AK; see also

735   Novellino et al., 2020). This post-collapse eruptive activity paused on Jan. 11th 2019, and Reynolds

736   (2019) was able to conduct a drone survey of AK and the islands of Rakata, Sertung and Panjang

737   (e.g., Fig. S1f and supplementary 4 in Grilli et al., 2019), that confirmed AK's coastline changes

738   inferred from SAR images. Arguably more important was their documentation of the large runups

739   the tsunami caused on the island of Rakata, Sertung and Panjang. Based on these images, Grilli et

740   al. (2019) estimated that 50+ m runups occurred on Rakata's N shore and Sertung's S shore.

741   Subsequent field surveys in 02/2019 by Borrero et al. (2020) and August 2019 by the authors

742   confirmed and quantified these early observations of near-field tsunami impact, and provided geo-

743   localized runup values reaching 80-85+ m on both islands (Fig. 11), with additional data on

744   Panjang. However, because Panjang was positioned downwind of AK, extensive ashfall-driven

745   vegetation damage, combined with the steep cliffs on the W coast (see white line in Fig. 11b) made

746   the runup line on Panjang difficult to unambiguously identify. Finally, Borrero et al. (2020) also

747   measured runup on Sebesi island, north of Panjang, which we also consider to be part of the near-

748   field tsunami impact (Fig. 1a).

749   For the likeliest collapse volume scenario, with granular material, Figures 12a-c show

750   zoom-ins of the maximum envelope of surface elevation computed with NHWAVE (Fig. 8) onto

751   the NW shore of Rakata, SW shore of Sertung and S shore of Panjang, and Fig. 12d shows a zoom-

752   in on Sebesi of the maximum envelope of surface elevation computed with FUNWAVE for the

753   same scenario (Fig. 9d). The location of our August 2019 drone tree line survey is marked on Figs.

754   12a,b, and the location of four runups/flow depth measurements made on Sebesi by Borrero et al.

755   (2019) are marked on Fig. 12d (7.5, 9, 2.8, 2.5 m from W to E, respectively); the latter values are

756   consistent with those we estimated during our August 2019 survey of Sebesi, in part based on

757   interviewing eyewitnesses. On both Rakata and Sertung (Figs. 12a,b), our predicted runup line

758   touches or goes over the 50 m contour and parallels the drone survey quite well, except at its

759   highest points; those however occur on steep, nearly vertical, cliff faces (Figs. 11a,c) that are not

760   well resolved with a 30 m horizontal grid. On Panjang, in Fig. 12c, our results show runups of 25-

761   30 m on the island's SW tip, tapering to 8-10 m on the NW part of the western shore; the latter

762   values match those reported by Borrero et al. (2020), who could not make a precise survey due to

763   the difficulty in accessing the island, which is faced by steep cliffs on much of its western side

764   (Fig. 11b). In Fig. 12d, our model results show a close agreement with the 4 measured runups on

765   Sebesi's S and SE shore.

766   Figure 13 details the near-field runups computed on the 3 islands for the 8 modeled

767   scenarios (4 volumes and 2 rheologies), compared to available runup measurements and our drone

768   surveys. Overall, on Rakata and Sertung (Figs 13a,b), although all scenarios fare quite well, the

769   likeliest volume scenario with a granular rheology appears to best match the quantitative field data,

770   as well as images from the 01/11/2019 and Borrerro's et al.'s (2020) 02/2019 field survey (Figs.

771   11d,e) of these islands. On Panjang (Fig. 13c), all our model results are below our tree line drone

772   survey (Fig. 11b) but, again, this was done along a nearly vertical cliff face, a location where it

773   was difficult to estimate the runup line precisely and which is not well-discretized in our model

774   grid; hence, there is large uncertainty on both these runup measurements and their model

775   simulation. We note that all scenarios predict an 8 m runup on the NW side of the island as was

776   reported by Borrero et al. (2020).

777

778   4.5 *Far-field runups*

779   Far-field flow depth and runups were measured along the coasts most exposed to the tsunami in

780   Java and Sumatra in several field surveys. The first one (TDMRC, 2019 took place in 01/2019,

781   soon after the event) was the only such data available to Grilli et al. (2019) to validate their

782 modeling. However, field surveys were also later performed by Muhari et al. (2019), Putra et al.

783 (2020), Borrero et al. (2020), and Heidarzadeh et al. (2020b). Figures 14 to 16 compare model

784 results obtained for the likeliest collapse scenario (granular rheology) with this data which, to our

785 knowledge, is all such data available to date.

786 　　　　Figure 14 shows a zoom-in along the coast of Java (Fig. 1a) on the envelope of maximum

787 surface elevation computed with FUNWAVE (Fig. 9d). As detailed in the methods section, both

788 the maximum flow depth at the shore and the runup were extracted from these results and, for

789 clarity, color coded in 4 classes of surface elevation. Due to the complex geometry of the coast,

790 the same values of flow depth and runup were then plotted as a function of longitude and latitude

791 in 4 subfigures (Figs. 14a,b,d,e); on the plan view (Fig. 14c), the color coded flow depth values

792 were plotted along the shore. Fig. 14c shows that, as expected from the tsunami directionality,

793 wave guiding effects offshore, and wave refraction nearshore, leading to focusing/defocusing

794 effects, the alongshore variation of maximum tsunami impact is a highly irregular on SW Java;

795 this causes similarly large alongshore variations in flow depth and runup seen in Figs. 14a,b,d,e.

796 The field data for both flow depth and runup is plotted on top of the elevation figures showing

797 model results, in Figs. 14b,d and. 14a,e, respectively. Overall, there is good agreement of model

798 results with the field measurements, and more so for flow depth at the coast, which is less sensitive

799 to irregularities of the terrain and the built-up elevation maps, that are not represented in our 50 m

800 resolution grid.

801 　　　　Figure 15 shows zoom-ins of results presented in Fig. 14 in three of the most impacted

802 areas along the coast of Java where field surveys were conducted, namely (Fig. 1a): (PI) Panaitan

803 Island; (UK) Ujung Kulon; and (K) Kolijaah. Model results for the likeliest volume scenario

804 (granular rheology) are compared to the locations/values of measured maximum runups, wherever

805   available (Fig. 15e), or otherwise to field data measured by Borrero et al. (2020) marked onto

806   Google Earth images of each site (Figs. 15b,d). These measurements were provided as raw or

807   detided, so here we are plotting their raw values compared to our results with respects to MWL.

808   [Note, Borrero et al. only assumed a 2 cm tide throughout without justification, which will

809   introduce some uncertainty in the comparison; also, their measurements from UK (Fig. 15d) are

810   reported on Figs 14a,e as runup, since these values were measured inland.] At PI (Figs. 15a,b),

811   the model accurately predicts the 6-8.4 m (referred to MWL) maximum tsunami elevations

812   measured at the marked locations along an approximate N to S survey from the tip of the island

813   (Fig. 15b; Borrero et al., 2020). At UK (Figs 15c,d) the model predicts slightly less (6.5 to 9 m)

814   than the 6.9-11.5 m range (referred to MWL) of maximum tsunami heights measured at the marked

815   locations from N to S from the tip of the Peninsula (Fig. 15d; Borrero et al, 2020); however, the

816   largest flow depth was measured at an isolated tree (their Fig. 12) and our 50 m resolution model

817   grid cannot represent this level of detail. Finally, at K (Figs. 15e,f) the model predicts most of the

818   runups (both location and value) measured by Muhari et al. (2019), Putra et al. (2020), and

819   Heidarzadeh et al. (2020b), reasonably well. Some of the reported measurement locations show a

820   mismatch, but the majority of measured runups in the 3 surveys align well with our predicted

821   inundation limit. At the K location, the Google Earth image (Fig. 15f) is only provided for

822   reference.

823   Figure 16 shows results similar to those of Figure 14, for flow depth at the coast predicted

824   along the SW shore of Sumatra for the likeliest collapse volume scenario (granular rheology),

825   compared to the available data from field surveys; the agreement between both is quite good here

826   as well. The largest tsunami impact occurred in the area of Waymuli (W in Fig. 1a, around

827 105.6348 E), of which Fig. 16c shows a picture of the damage taken by Fritz et al. (2019) during

828 their 02/2019 survey.

829

830 **5 Discussion and conclusions**.

831 New numerical simulations of AK's 2018 collapse and tsunami generation, propagation,

832 and coastal impact were performed with state-of-the-art numerical models, including a novel

833 landslide tsunami model for granular and viscous slides that includes non-hydrostatic effects of

834 vertical acceleration in the slide material. Results show that incorporating non-hydrostatic effects

835 is important for accurately simulating tsunami generation and near-field impacts from the AK flank

836 collapse. This is illustrated in the 8 scenarios we used, which combined 2 different rheologies

837 (granular and viscous fluid material) and 4 different volumes obtained from a new parametrization

838 of the collapse based on our August 2019 marine hydroacoustic survey (cf. Hunt et al., 2021), field

839 observations and new interpretations of high-resolution satellite imagery.

840 Based on our improved knowledge/understanding of subaerial and submarine data, from

841 which we better constrained the geometry and magnitude of the landslide mechanism, we also

842 improved on previous interpretations of the primary landslide scar, which bisected the Anak

843 Krakatau edifice, cutting behind the central vent and removing 50% of its subaerial volume. The

844 combined subaerial and marine datasets presented in Hunt et al. (2021) are used to provide a better

845 validated estimate of the landslide failure volume. From this, the failure volume is estimated to lie

846 within a range of 0.175 to 0.313 km^3, spanning the independently estimated deposit volume of

847 0.214 km^3. Given uncertainties in the precise form of the failure plane, the likeliest failure volume

848 of 0.224 km^3 is defined based on the submarine blocky deposit volume, mapped in the deep basin

849 to the SW of AK (0.214 ± 0.036 km^3) and allowing for an additional contribution from a much

850 smaller volume (0.022 ± 0.006 km^3) secondary debris flow deposit also mapped SW of the main

851 blocky deposit. Alongside this, we also model three additional failure scenarios encompassing the

852 minimum and maximum bounds of the landslide failure surface and geometry, with the 4 collapse

853 scenario geometries having volumes between 0.175 and 0.313 km^3.

854   Observations of a single tsunami wave train, with no subsequently generated waves, are

855 consistent with our interpretation from the marine surveys of landslide failure as a rapid, single

856 phase, *en masse* movement, rather than a more piecemeal process; in the seafloor deposits, there

857 is indeed no evidence that the slide volume was divided among multiple-stages of failure (Hunt et

858 al., 2021). A single event interpretation is also supported by the marine seismic data. Thus, unlike

859 the collapses at larger volcanic islands (e.g., Canaries; Hunt et al., 2011), single-stage failures that

860 maximize the volume of material available at any one time for tsunamigenesis appear to be more

861 the norm in settings such as AK's.

862   In the context of the many uncertainties in field observations, all our volume scenarios

863 successfully reproduced the near- and far-field tsunami flow depths and runups observed in all

864 post-event field survey results published to date, as well as arrival times and time series of surface

865 elevations at tide gauges, and from eyewitness reports. This match between our model results and

866 field observations confirms that our estimated landslide volume range and material rheologies are

867 appropriate to the collapse event. Note, however, that slide dilation, an important physical aspect,

868 which results from water being sucked into the granular material during slide motion, is not

869 included in NHWAVE. While this effect could affect tsunami generation, the good agreement

870 observed in the near-field between the measured and predicted runups would indicate that this was

871 not significant during AK's event. Additionally, the many large blocks seen in the debris deposits

872 would indicate that the amount of interstitial water may have been smaller than assumed in

873　simulations and that actual dilation effects were minor. Nevertheless dilation would be important

874　to include in the model and study in future work.

875　　Despite an observed moderate sensitivity of tsunami impact to the range of modeled

876　landslide sources, particularly in the far-field, the granular rheology appears to yield slide deposits

877　in better agreement with the marine deposits mapped in the 2019 survey (both location and

878　thickness) than those from the dense fluid rheology. Additionally, near-field runups are also better

879　predicted using a granular rheology. Regarding the collapse volume, the likeliest value inferred

880　from the 2019 field survey, together with a refined analysis of satellite images, is 0.224 km^3

881　(referred to in this paper as the likeliest scenario), which appears to provide the overall best

882　agreement with the near-field runup measurements, as well as the far-field data. Hence, while the

883　volume is harder to constrain using far-field data, we conclude that tsunami modeling supports the

884　likeliest scenario inferred from the 2019 marine geology survey, although the constraint is weaker

885　than for the rheology.

886　　The AK event highlights the significant hazard posed by relatively small-scale lateral

887　volcanic collapses, which occur *en-masse*, without any readily identified 'predictive', precursory

888　signals, and are an efficient and unpredictable tsunami source. Our successful simulations

889　demonstrate that current numerical models can accurately forecast tsunami hazards from these

890　events, even assuming a large uncertainty on the source parameters (e.g., collapse failure plane

891　and volume); this is why Giachetti et al. (2012)'s work provided a reasonable forecast of the event

892　that took place at AK in 2018.

893　　In cases such as AK's, the absence of precursory warning signals of imminent collapse

894　together with the short travel time following tsunami initiation present a major challenge for

895　mitigating tsunami coastal impact from volcanic sources, stressing the need to install early warning

896   systems. After the AK 2018 event, using ground- and space-borne data, Walter et al. (2019)

897   identified thermal anomalies and a gradual seaward motion of the volcano that they suggested

898   could be used as precursors of the collapse. A warning system could thus closely monitor

899   volcanoes exhibiting and elevated sate of activity for such precursor signs. Warning systems could

900   also use instruments allowing for an early detection of the tsunami generated by the collapse. Mulia

901   et al. (2020) suggested that a high frequency (HF) radar could have been useful in providing an

902   early detection of the tsunami generated by AK's collapse. In fact, Grilli et al. (2016, 2017a)

903   proposed new algorithms for processing HF radar data to efficiently detect tsunami signals; by

904   performing model simulations similar to those reported here, they demonstrated that their

905   algorithm could provide an early detection of landslide tsunamis. Guérin et al. (2018) later applied

906   this method to detect a meteo-tsunami/surge using actual HF radar data, off of Toffino, BC.

907   Another novel approach recently proposed for detecting sea surface variations, such as those

908   caused by non-seismic tsunamis, is that based on Coastal Global Navigation Satellite Systems

909   (GNSS) signal reflection on the sea surface (e.g., Larson et al., 2020).

910

911   **Data sharing**

912   A shared Google Drive folder containing all the NHWAVE and FUNWAVE model input data as

913   well as all raw results generated for the simulations of the 2018 AK collapse and tsunami reported

914   in   this   paper   is   accessible   at: https://drive.google.com/drive/folders/1-60PsB3Zj-

915   P58rbbAdbWUZ611I_QMs2S?usp=sharing.

916

917   **Acknowledgements**

References

1. Abadie, S.M., Harris, J.C., Grilli, S.T. & Fabre, R. (2012). Numerical modeling of tsunami waves generated by the flank collapse of the Cumbre Vieja Volcano (La Palma, Canary Islands): Tsunami source and near field effects. Journal of Geophysical Research, vol. 117, pp. C05030, doi:10.1029/2011jc007646.

2. Abadie, S., Paris, A., Ata, R., Le Roy, S., Arnaud, G., Poupardin, A., Clous, L., Heinrich, P., Harris, J., Pedreros, R. and Krien, Y. (2020). La Palma landslide tsunami: calibrated wave source and assessment of impact on French territories. Natural Hazards and Earth System Sciences, vol. 20, no. 11, pp. 3019-3038, doi:10.5194/nhess-20-3019-2020.

3. Abdurrachman, M., Widiyantoro, S., Priadi, B., Ismail, T. (2018). Geochemistry and Structure of Krakatoa Volcano in the Sunda Strait, Indonesia. Geosciences, vol. 8, pp. 111.

4. AGU blog 2019. Anak Krakatau: Planet Labs imagery of the aftermath of the landslide. Accessed Jan. 3, 2019. https://blogs.agu.org/landslideblog/2019/01/03/anak-krakatau-3/?utm_source=AGU+Blogosphere+-+The+Landslide+Blog&utm_campaign=0979aaaa17-RSS_EMAIL_CAMPAIGN_LANDSLIDE&utm_medium=email&utm_term=0_b2461e255e-0979aaaa17-555513653

5. AHA, C. (2018). Indonesia, Tsunami in Sunda Strait, http://adinet.ahacentre.org/reports/view/1383. First accessed Dec. 23, 2018.

6. Andersen, O. (2018). Krakatau Volcano: Witnessing the eruption, tsunami and the aftermath 22-23th December 2018, Accessed on December 26, 2018. http://www.oysteinlundandersen.com/krakatau-volcano-witnessing-the-eruption-tsunami-22december2018/.

7. Anon (2018). Global Volcanic Program, in: Venzke, E. (Ed.), Bulletin of the Global Volcanism Network. Smithsonian Institution, Washington.

958   8.   Auker, M.R., Sparks, R.S.J., Siebert, L., Crosweller, H.S., Ewert, J. (2013). A statistical analysis of the

959   global historical volcanic fatalities record. Journal of Applied Volcanology, vol. 2, pp. 1-24,

960   doi:10.1186/2191-5040-2-2.

961   9.   Borrero, J.C., T. Solihuddin, H.M. Fritz, P.J. Lynett, G.S. Prasetya, D. Purbani, H.L Salim et al. (2020).

962   Field Survey and Numerical Modelling of the December 22, 2018 Anak Krakatau Tsunami. Pure and

963   Applied Geophys., vol. 177, pp. 2457-2475, doi:10.1007/s00024-020-02515-y

964   10. Camus, G., Gourgaud, A., Vincent, P.M. (1987). Petrologic evolution of Krakatau (Indonesia):

965   Implications for a future activity. Journal of Volcanology and Geothermal Research, vol. 33, pp. 299-

966   316, doi:10.1016/0377-0273(87)90020-5.

967   11. Day, S.J., P. Watts, S.T. Grilli and Kirby J.T. (2005). Mechanical Models of the 1975 Kalapana, Hawaii

968   Earthquake and Tsunami. Marine Geology, vol. 215, no. 1-2, pp. 59-92,

969   doi:10.1016/j.margeo.2004.11.008.

970   12. Day, S. (2015). Volcanic tsunamis, The Encyclopedia of Volcanoes. Elsevier, pp. 993–1009.

971   13. Day, S., Lanes, P., Silver, E., Hoffmann, G., Ward, S., Driscoll, N. (2015). Submarine landslide

972   deposits of the historical lateral collapse of Ritter Island, Papua New Guinea. Marine and Petroleum

973   Geology, vol. 67, pp. 419-438, doi:10.1016/j.marpetgeo.2015.05.017.

974   14. Deplus, C., S. Bonvalot, D. Dahrin, M. Diament, H. Harjono, and J. Dubois (1995). Inner structure of

975   the Krakatau volcanic complex (Indonesia) from gravity and bathymetry data. J. Volcan. Geotherm.

976   Res., vol. 64, no. 1-2, pp. 23-52, doi:10.1016/0377-0273(94)00038-I.

977   15. Dogan, G.G., Annunziato, A., Hidayat, R., Husrin, S., Prasetya, G., Kongko, W., Zaytsev, A.,

978   Pelinovsky, E., Imamura, F. and Yalciner, A.C. (2021). Numerical Simulations of December 22, 2018

979   Anak Krakatau Tsunami and Examination of Possible Submarine Landslide Scenarios. Pure and

980   Applied Geophysics, pp.1-20, doi:10.1007/s00024-020-02641-7.

981   16. Fritz et 16 alii (2019). The 2018 Anak Krakatau tsunami: Near-source field survey on Islands in the

982   Sunda Strait. Presentation at Intl. Symp. on the Lessons Learnt from the 2018 Tsunamis in Palu and

983   Sunda Strait, 26-28 September 2019, Auditorium BMKG, Jakarta – Indonesia.

984 17. Fornaciai, A., Favalli, M. and Nannipieri, L. (2019). Numerical simulation of the tsunamis generated

985 by the Sciara del Fuoco landslides (Stromboli Island, Italy). Scientific reports, vol. 9, no. 1, pp. 1-12,

986 doi: 10.1038/s41598-019-54949-7.

987 18. Giachetti, T., Paris, R., Kelfoun, K., Pérez-Torrado, F.J. (2011). Numerical modelling of the tsunami

988 triggered by the Güimar debris avalanche, Tenerife (Canary Islands): Comparison with field-based data.

989 Marine Geology, vol. 284, pp. 189-202, doi:10.1016/j.margeo.2011.03.018.

990 19. Giachetti, T., Paris, R., Kelfoun, K., Ontowirjo, B. (2012). Tsunami hazard related to a flank collapse

991 of Anak Krakatau Volcano, Sunda Strait, Indonesia. Geological Society, London, Special Publications,

992 vol. 361, pp. 79-90.

993 20. Glimsdal, S., Pedersen, G. K., Harbitz, C. B., and Løvholt, F. (2013). Dispersion of tsunamis: does it

994 really matter? Natural hazards and earth system sciences, vol. 13, no. 6, pp. 1507-1526, doi:

995 10.5194/nhess-13-1507-2013.

996 21. Gouhier, M. and Paris, R (2019). SO2 and tephra emissions during the December 22, 2018 Anak

997 Krakatau eruption. Volcanica, vol. 2, no. 2, pp. 91-103, doi: 10.30909/vol.02.02.91103.

998 22. Grilli, S.T., Ioualalen, M, Asavanant, J., Shi, F., Kirby, J. and Watts, P. (2007). Source Constraints and

999 Model Simulation of the December 26, 2004 Indian Ocean Tsunami. Journal of Waterway Port Coastal

1000 and Ocean Engineering, vol. 133, no. 6, pp. 414-428, doi:10.1061/(ASCE)0733-

1001 950X(2007)133:6(414).

1002 23. Grilli, S.T. J.C. Harris, T. Tajalibakhsh, T.L. Masterlark, C. Kyriakopoulos, J.T. Kirby and F. Shi

1003 (2013). Numerical simulation of the 2011 Tohoku tsunami based on a new transient fem co-seismic

1004 source: Comparison to far- and near-field observations. Pure and Applied Geophysics, vol. 170, pp.

1005 1333–1359, doi:10.1007/s00024-012-0528-y.

1006 24. Grilli, S.T., O'Reilly, C., Harris, J.C., Tajelli-Bakhsh, T., Tehranirad, B., Banihashemi, S., Kirby, J.T.,

1007 Baxter, C.D.P., Eggeling, T., Ma, G., and F. Shi (2015). Modeling of SMF tsunami hazard along the

1008 upper US East Coast: detailed impact around Ocean City, MD. Natural Hazards, vol. 76, pp. 705-746;

1009 doi:10.1007/s11069-014-1522-8.

1010   25. Grilli, S.T., Grosdidier S. and C.-A. Guérin (2016). Tsunami detection by High Frequency Radar

1011   beyond the continental shelf. I. Algorithms and validation on idealized case studies. Pure and Applied

1012   Geophysics, vol. 173, no. 12, pp. 3,895-3,934, doi:10.1007/s00024-015-1193-8

1013   26. Grilli, S.T., Guérin, C.-A., Shelby, M., Grilli, A., P. Moran, Grosdidier, S. and T.L. Insua (2017a).

1014   Tsunami detection by High Frequency Radar beyond the continental shelf: II. Extension of algorithms

1015   and validation on realistic case studies. Pure and Appl. Geophys., vol. 174, no. 1, pp. 3,003-

1016   3,028, doi:10.1007/s00024-017-1619-6.

1017   27. Grilli, S.T., Shelby, M., Kimmoun, O., Dupont, G., Nicolsky, D., Ma, G., Kirby, J.T. and F. Shi

1018   (2017b). Modeling coastal tsunami hazard from submarine mass failures: effect of slide rheology,

1019   experimental validation, and case studies off the US East coast. Natural Hazards, vol. 86(1), pp. 353-

1020   391, doi:10.1007/s11069-016-2692-3.

1021   28. Grilli, S.T., Tappin, D.R., Carey, S., Watt, S.F.L., Ward, S.N., Grilli, A.R., Engwell, S.L., Zhang, C.,

1022   Kirby, J.T., Schambach, L., Muin, M. (2019). Modelling of the tsunami from the December 22, 2018

1023   lateral collapse of Anak Krakatau volcano in the Sunda Straits, Indonesia. Scientific Reports, vol. 9,

1024   no. 11946, doi:10.1038/s41598-019-48327-6.

1025   29. Guérin C.-A., S.T. Grilli, P. Moran, A.R. Grilli, T.L. Insua (2018). Tsunami detection by High

1026   Frequency Radar in British Columbia: performance assessment of the Time-Correlation Algorithm for

1027   synthetic and real events. Ocean Dynamics, 68(4-5), pp. 423-438, doi:10.1007/s10236-018-1139-7.

1028   30. Gurney, J. (2018) Low frequency analysis of the 13:55 event (arrival at Bungbulang at 13:57 UTC),

1029   UK Earthquake Bulletin.

1030   31. Heidarzadeh, M., Ishibe, T., Sandanbata, O., Muhari, A., Wijanarto, A.B. (2020a). Numerical modeling

1031   of the subaerial landslide source of the 22 December 2018 Anak Krakatoa volcanic tsunami, Indonesia.

1032   Ocean Engineering, vol. 195, no. 106733.

1033　32. Heidarzadeh, M., Putra, P. S., Nugroho, S. H., and Rashid, D. B. Z. (2020b). Field survey of tsunami

1034　　　heights and runups following the 22 December 2018 Anak Krakatau volcano tsunami, Indonesia. Pure

1035　　　and Applied Geophysics, vol. 177, no. 10, pp. 4577-4595, doi: 10.1016/j.oceaneng.2019.106733

1036　33. Hunt, J.E., Wynn, R.B., Masson, D.G., Talling, P.J., Teagle, D.A.H. (2011). Sedimentological and

1037　　　geochemical evidence for multistage failure of volcanic island landslides: A case study from Icod

1038　　　landslide on north Tenerife, Canary Islands. Geochem. Geophys. Geosyst., vol. 12, no. Q12007, doi:

1039　　　10.1029/2011GC003740

1040　34. Hunt, J.E., Tappin, D.R., Watt, S.F., Susilohadi, S., Novellino, A., Ebmeier, S.K., Cassidy, M.,

1041　　　Engwell, S.L., Grilli, S.T., Hanif, M., Priyanto, W.S., Clare, M.A., Abdurrachman, M., Udrekh, U.

1042　　　(2021). Submarine landslide megablocks show half the island of Anak Krakatau failed on December

1043　　　22nd, 2018. Nature Communication, vol. 12, no. 2827, doi:10.1038/S41467-021-22610-5.

1044　35. Imamura, F. and Imteaz, M.M.A. (1995). Long waves in two-layers: Governing equations and

1045　　　numerical model. Science of Tsunami Hazards, vol. 13, no. 1, pp. 3-24.

1046　36. Ina-COAP (2019). *Tide Gauge data in Indonesia*, http://tides.big.go.id/las/UI.vm Accessed Jan. 3,

1047　　　2019.

1048　37. Ioualalen, M., Asavanant, J., Kaewbanjak, N., Grilli, S.T., Kirby, J.T. and P. Watts (2007). Modeling

1049　　　the 26th December 2004 Indian Ocean tsunami: Case study of impact in Thailand. Journal of

1050　　　Geophysical Research, vol. 112, pp. C07024, doi:10.1029/2006JC003850.

1051　38. Johnson, R.W., (1987). Large-scale volcanic cone collapse: the 1888 slope failure of Ritter Volcano,

1052　　　and other examples from Papua New Guinea. Bulletin of Volcanology, vol. 49, pp. 669–679, doi:

1053　　　10.1007/BF01080358.

1054　39. Karstens, J., Berndt, C., Urlaub, M., Watt, S.F.L., Micallef, A. et al. (2019). From gradual spreading to

1055　　　catastrophic collapse – Reconstruction of the 1888 Ritter Island volcanic sector collapse from high-

1056　　　resolution 3D seismic data. Earth and Planetary Science Letters, vol. 517, pp. 1-13, doi:

1057　　　10.1016/j.epsl.2019.04.009

1058   40. Kirby, J.T., Shi, F., Tehranirad, B., Harris, J.C. and Grilli, S.T. (2013). Dispersive tsunami waves in

1059   the ocean: Model equations and sensitivity to dispersion and Coriolis effects. Ocean Modeling, vol. 62,

1060   pp. 39-55, doi:10.1016/j.ocemod.2012.11.009.

1061   41. Kirby, J.T., Shi, F., Nicolsky, D., and S. Misra (2016). The 27 April 1975 Kitimat, British Colombia,

1062   submarine landslide tsunami: a comparison of modeling approaches. Landslides, vol. 13, no. 6, pp.

1063   1421-1434 doi: 10.1007/s10346-016-0682-x.

1064   42. Larson, K. M., Lay, T., Yamazaki, Y., Cheung, K. F., Ye, L., Williams, S. D. and Davis, J. L. (2021).

1065   Dynamic sea level variation from GNSS: 2020 Shumagin earthquake tsunami resonance and Hurricane

1066   Laura. Geophysical Research Letters, vol. 48, no. 4, e2020GL091378, doi: 10.1029/2020GL091378 .

1067   43. Løvholt, F., Pedersen, G., Gisler, G. (2008). Oceanic propagation of a potential tsunami from the La

1068   Palma Island. Journal of Geophysical Research, vol. 113, no. C09026, doi:10.1029/2007JC004603.

1069   44. Ma, G., Shi, F., and Kirby, J.T. (2012). Shock-capturing non-hydrostatic model for fully dispersive

1070   surface wave processes. Ocean Modelling, vol. 43-44, pp. 22-35, doi:10.1016/j.ocemod.2011.12.002.

1071   45. Ma, G., Kirby, J.T., Hsu, T.J., and Shi, F. (2015). A two-layer granular landslide model for tsunami

1072   wave   generation: theory   and   computation.   Ocean   Modelling,   vol.   93,   pp.   40-55,

1073   doi:10.1016/j.ocemod.2015.07.012.

1074   46. Muhari,   A.   (2018).   in   *Kompas*,   (in   Indonesian)

1075   https://sains.kompas.com/read/2018/12/23/180319123/menyoal-dakwaan-pada-anak-krakatau-

1076   tentang-kasus-tsunami-selat-sunda?page=all. Accessed Dec. 23, 2018.

1077   47. Muhari, A., Heidarzadeh, M., Susmoro, H., Nugroho, H.D., Kriswati, E., Wijanarto, A.B., Imamura, F.

1078   and Arikawa, T. (2019). The December 2018 Anak Krakatau volcano tsunami as inferred from post-

1079   tsunami field surveys and spectral analysis. Pure and Applied Geophysics, vol. 176, no. 12, pp. 5219-

1080   5233, doi: https:10.1007/s00024-019-02358-2.

1081   48. Mulia, I.E., Watada, S., Ho, T.-C., Satake, K., Wang, Y., Aditiya, A. (2020). Simulation of the 2018

1082   Tsunami Due to the Flank Failure of Anak Krakatau Volcano and Implication for Future Observing

1083   Systems. Geophysical Research Letters, vol. 47, no. e2020GL087334, doi:10.1029/2020GL087334.

1084   49. Neumann van Padang, M. (1983). History of the volcanology in the former Netherlands East Indies. *Rijksmuseum van Geologie en Mineralogie.*

1086   50. Novellino, A., Engwell, S.L., Grebby, S., Day, S., Cassidy, M., Madden-Nadeau, A., Watt, S., Pyle, D., Abdurrachman, M., Edo Marshal Nurshal, M. and Tappin, D.R. (2020). Mapping recent shoreline changes spanning the lateral collapse of Anak Krakatau Volcano, Indonesia. Appl. Sci., vol. 10, no. 2, pp. 536, doi: 10.3390/app10020536.

1090   51. Omira, R. and Ramalho, I. (2020). Evidence-Calibrated Numerical Model of December 22, 2018, Anak Krakatau Flank Collapse and Tsunami. Pure and Applied Geophysics, vol. 177, no. 7, pp. 3059-3071, doi: 10.1007/s00024-020-02532-x.

1093   52. Paris, R. (2015). Source mechanisms of volcanic tsunamis. Philosophical Transactions of the Royal Society of London A: Mathematical, Physical and Engineering Sciences, vol. 373, no. 2053, pp. 20140380, doi: 10.1098/rsta.2014.0380.

1096   53. Paris, A., Heinrich, P., Paris, R., and Abadie, S. (2020a). The December 22, 2018 Anak Krakatau, Indonesia, landslide and tsunami: preliminary modeling results. Pure and Applied Geophysics, vol. 177, no. 2, pp. 571-590, doi: 10.1007/s00024-019-02394-y

1099   54. Paris, R., Goto, K., Goff, J. and Yanagisawa, H. (2020b). Advances in the study of mega-tsunamis in the geological record. Earth-Science Reviews, no. 103381, doi:10.1016/j.earscirev.2020.103381.

1101   55. Perttu, A., Caudron, C., Assink, J.D., Metz, D., Tailpied, D., Perttu, B., Hibert, C., Nurfiani, D., Pilger, C., Muzli, M. and Fee, D. (2020). Reconstruction of the 2018 tsunamigenic flank collapse and eruptive activity at Anak Krakatau based on eyewitness reports, seismo-acoustic and satellite observations. Earth and Planetary Science Letters, vol. 541, pp.116268, doi: 10.1016/j.epsl.2020.116268.

1106   56. Putra, P. S., Aswan, A., Maryunani, K. A., Yulianto, E., Nugroho, S. H., & Setiawan, V. (2020). Post-Event Field Survey of the 22 December 2018 Anak Krakatau Tsunami. Pure and Applied Geophysics, vol. 177, pp. 2477–2492, doi:10.1007/s00024-020-02446-8

1109   57. PVMBG (2018). Activity reports for Anak Krakatau from 01/12/2018 – 03/01/2019. Pusat Vulkanologi
1110   dan Mitigasi Bencana Geologi.

1111   58. Priyanto, W.S., Hunt, J.E., Hanif, M., Tappin, D.R., Permana, H., Susilohadi, S., Cassidy, M. and
1112   Yulianto, E. (2021). Bathymetry and Shallow Seismic Imaging of the 2018 Flank Collapse of Anak
1113   Krakatau. Frontiers in Earth Science, 8, pp. 649, doi:10.3389/feart.2020.577448.

1114   59. Ren, Z., Wang, Y., Wang, P., Hou, J., Gao, Y., and Zhao, L. (2020). Numerical study of the triggering
1115   mechanism of the 2018 Anak Krakatau tsunami: eruption or collapsed landslide?. Natural Hazards, vol.
1116   102, no. 1, pp. 1-13, doi:10.1007/s11069-020-03907-y.

1117   60. Reynolds, J. (2019). *Post-collapse image of Anak Krakatau. Earth Uncut TV*,
1118   https://twitter.com/hashtag/Krakatau?src=hash, Accessed Jan. 11, 2019.

1119   61. Schambach L., Grilli S.T., Kirby J.T. and F. Shi (2019). Landslide tsunami hazard along the upper US
1120   East Coast: effects of slide rheology, bottom friction, and frequency dispersion. Pure and Applied
1121   Geophys*ics*, vol. 176, no. 7, pp. 3,059-3,098, doi.org/10.1007/s00024-018-1978-7.

1122   62. Schambach L., Grilli S.T., Tappin D.R., Gangemi M.D., and G. Barbaro (2020a). New simulations and
1123   understanding of the 1908 Messina tsunami for a dual seismic and deep submarine mass failure
1124   source, *Marine Geology*, vol. 421, pp. 106093, doi: 10.1016/j.margeo.2019.106093.

1125   63. Schambach L., Grilli S.T. and D.R. Tappin (2020b). New high-resolution modeling of the 2018 Palu
1126   tsunami, based on supershear earthquake mechanisms and mapped coastal landslides, supports a dual
1127   source. Frontiers in Earth Sciences, vol. 8, pp. 627, doi:10.3389/feart.2020.598839.

1128   64. Simkin, T., Fiske, R.S. (1983). Krakatau 1883: the volcanic eruption and its effects. Smithsonian
1129   Institution Press, Washington, D.C.

1130   65. Siswowidjoyo, S. (1983). Krakatau, Symposium on 100 years development Krakatau its surroundings.
1131   Indonesian Inst. Sci. Jakarta, Jakarta, pp. 191–198.

1132   66. Shi, F., Kirby, J.T., Harris, J.C., Geiman, J.D. and S.T. Grilli (2012). A high-order adaptive time-
1133   stepping TVD solver for Boussinesq modelling of breaking waves and coastal inundation. Ocean
1134   Modelling, vol. 43-44, pp. 36-51, doi:10.1016/j.ocemod.2011.12.004.

1135   67. Stehn, C. (1929). The geology and volcanism of the Krakatau group, Krakatau, Proc. 4th Pacific Sci.

1136   Congr, Batavia I, pp. 1-55.

1137   68. Tappin, D.R., Watts, P., Grilli, S.T. 2008. The Papua New Guinea tsunami of 1998: anatomy of a

1138   catastrophic event. Natural Hazards and Earth System Sciences, vol. 8, pp. 243-266, doi:www.nat-

1139   hazards-earth-syst-sci.net/8/243/2008/

1140   69. Tappin, D.R., Grilli, S.T., Harris, J.C., Geller, R.J., Masterlark, T., Kirby, J.T., Shi, F., Ma, G.,

1141   Thingbaijam, K.K.S., and P.M. Mai (2014). Did a submarine landslide contribute to the 2011 Tohoku

1142   tsunami? Marine Geology, vol. 357, pp. 344-361, doi:10.1016/j.margeo.2014.09.043.

1143   70. TDMRC (Tsunami, D., and Mitigation, Research, Center) (2019). Post Sunda Strait Tsunami Survey.

1144   Tsunami, Disaster, and Mitigation, Research, Center, Jakarta. http://tdmrc.unsyiah.ac.id/thelatest-

1145   update-from-post-sunda-strait-tsunami-survey/. Accessed Jan. 8, 2019

1146   71. Tehranirad B., Harris J.C., Grilli A.R., Grilli S.T., Abadie S., Kirby J.T. and F. Shi 2015. Far-field

1147   tsunami impact in the north Atlantic basin from large scale flank collapses of the Cumbre Vieja volcano,

1148   La Palma. Pure and Applied Geophysics, vol. 172, no. 12, pp. 3,589-3,616, doi:10.1007/s00024-015-

1149   1135-5.

1150   72. Tinti, S., Pagnoni, G., and Zaniboni, F. (2006). The landslides and tsunamis of the 30th of December

1151   2002 in Stromboli analysed through numerical simulations. Bull. Volcanol. 68, 462–479.

1152   doi:10.1007/839 s00445-005-0022-9.

1153   73. Umbgrove, J. H. F. (1928). The first days of the new submarine volcano near Krakatoa. Leidse

1154   Geologische Mededelingen, vol. 2, no. 1, pp. 325-328.

1155   74. Verbeek, R.D.M. (1885). Krakatau. Government Press Batavia.

1156   75. Verbeek, R.D.M. (1983). Krakatau, in: Simkin, T., Fiske, R.S. (Eds.), Krakatau 1883: The Volcanic

1157   Eruption and its Effects. Smithsonian Press, Washington, D.C., pp. 169-277.

1158   76. Walter, T.R., Haghighi, M.H., Schneider, F.M., Coppola, D., Motagh, M., Saul, J., Babeyko, A., Dahm,

1159   T., Troll, V.R., Tilmann, F. and Heimann, S., 2019. Complex hazard cascade culminating in the Anak

1160   Krakatau sector collapse. Nature communications, vol. 10, no. 4339.

1161 77. Ward, S.N., Day, S. (2001). Cumbre Vieja volcano – Potential collapse and tsunami at La Palma,

1162   Canary Islands. Geophysical Research Letters, vol. 28, no. 17, pp. 3397– 3400, doi:

1163   10.1029/2001GL013110.

1164 78. Ward, S.N. and Day, S. (2003). Ritter Island Volcano-lateral collapse and the tsunami of 1888.

1165   Geophysical Journal International, vol. 154, pp. 891–902, doi: 10.1046/j.1365-246X.2003.02016.x.

1166 79. Ward, S. N. and Day, S. (2006). Particulate kinematic simulations of debris avalanches: interpretation

1167   of deposits and landslide seismic signals of Mount Saint Helens, 1980 May 18. Geophysical Journal

1168   International, vol. 167, no. 2, pp. 991-1004.

1169 80. Watt, S.F.L., Karstens, J., Micallef, A., Berndt, C., Urlaub, M., Ray, M., Desai, A., Sammartini, M.,

1170   Klaucke, I., Böttner, C., Day, S., Downes, H., Kühn, M., Elger, J. (2019). From catastrophic collapse

1171   to multi-phase deposition: Flow transformation, seafloor interaction and triggered eruption following a

1172   volcanic-island landslide. Earth and Planetary Science Letters, vol. 517, pp. 135-147, doi:

1173   10.1016/j.epsl.2019.04.024.

1174 81. Williams, R., Rowley, P. and Garthwaite, M.C. (2019). Reconstructing the Anak Krakatau flank

1175   collapse that caused the December 2018 Indonesian tsunami. Geology, vol. 47, no. 10, pp. 973-976,

1176   doi: 10.1130/G46517.1.

1177 82. Yavari-Ramshe, S., and Ataie-Ashtiani, B. (2016). Numerical simulation of subaerial and submarine

1178   landslide generated tsunami waves—recent advances and future challenges. Landslides, 13(6), pp.

1179   1325–1368, doi: 10.1007/s10346-016-0734-2.

1180 83. Ye, L., Kanamori, H., Rivera, L., Lay, T., Zhou, Y., Sianipar, D., and Satake, K. (2020). The 22

1181   December 2018 tsunami from flank collapse of Anak Krakatau volcano during eruption. Sci. Advances,

1182   vol. 6, no. 3, pp. eaaz1377, doi:10.1126/sciadv.aaz1377.

1183 84. Zengaffinen, T., Løvholt, F., Pedersen, G.K., Muhari, A. (2020). Modelling 2018 Anak Krakatoa Flank

1184   Collapse and Tsunami: Effect of Landslide Failure Mechanism and Dynamics on Tsunami Generation.

1185   Pure and Applied Geophysics, vol. 177, pp. 2493-2516, doi: 10.1007/s00024-020-02489-x.

1186   85. Zhang C., Kirby J., Shi F., Ma G. and S.T. Grilli (2021a). A two-layer non-hydrostatic landslide model

1187   for tsunami generation on irregular bathymetry. 1. Theoretical basis. *Ocean Modelling*, vol. 159, no.

1188   101749, doi:10.1016/j.ocemod.2020.101749.

1189   86. Zhang C., Kirby J., Shi F., Ma G. and S.T. Grilli (2021b). A two-layer non-hydrostatic landslide model

1190   for tsunami generation on irregular bathymetry. 2. Numerical discretization and model

1191   validation. *Ocean Modelling,* vol. 160, no. 101769, doi:10.1016/j.ocemod.2021.101769.

Tables

Study/Paper	AK Collapse model	Tsunami model	Bathymetry Grid	AK Collapse source
Grilli et al. (2019)	NHWAVE: Multi-layer 3D Euler solver coupled with 2D layer slide model with dense viscous fluid/granular medium slide rheology	FUNWAVE: 2D fully nonlinear and dispersive Boussinesq model	NHWAVE: 90 m resolution Cartesian grid with 5 vertical layers; FUNWAVE: 100 m resolution Cartesian grid. Bathy/topo: 100 m resolution Giachetti et al. (2012)'s data	Geometry and failure surface reconstructed from pre-/post-collapse satellite observations, with volume of 0.22-0.30 km^3 (likeliest 0.27 km^3)
Zengaffinen et al. (2020)	BinClaw: 2D two-layer water/slide coupled with viscoplastic slide rheology	GeoClaw: 2D nonlinear and non-dispersive long wave model (NLSW) GloBous: 2D linear dispersive long wave model (LSW) for limited comparison	BinClaw: 36 m resolution Cartesian grid GeoClaw: 175 m resolution Cartesian grid Globous: 100 m resolution Cartesian grid Bathy/topo: Giachetti et al. (2012)'s data	Same 0.28 km^3 volume, geometry, and failure surface as in Giachetti et al. (2012)
Paris et al. (2020a)	AVALANCHE: 2D two-layer water/slide with granular medium slide rheology	2D weakly nonlinear and dispersive Boussinesq model	Coarse grids (180 m ?) over deep water and 25 m resolution around AK and in 5 nested coastal grids Bathy/topo: from Gouhier and Paris (2019)	Geometry and failure surface reconstructed from pre-/post-collapse satellite and aerial observations, with volume of 0.15 km^3
Ren et al. (2020)	2D two-layer water/slide coupled model with dense fluid slide rheology	GeoClaw: 2D nonlinear and non-dispersive long wave model (NLSW)	Generation: 30 m resolution nested grid GeoClaw: Coarse 0.125 arc-min (230 m) resolution grid Bathy/topo: interpolated from coarse 30 arc-sec (900 m) SRTM30_Plus data	Geometry and failure surface reconstructed from pre-/post-collapse satellite observations, with volume of 0.10-0.30 km^3 based on Grilli et al. (2019)
Mulia et al. (2020)	VolcFlow: 2D two-layer water/slide coupled model simulating silde with avalanche dynamics with retarding stress	FUNWAVE: 2D fully nonlinear and dispersive Boussinesq model	VolcFlow: 3 arc-sec (90 m) resolution grid FUNWAVE: 6 arc-sec (180 m) resolution grid Bathy/topo: 6 arc-sec bathymetry and 0.27 arc-sec topography around AK	Similar failure surface as in Giachetti et al. (2012) with steeper plane yielding a 0.24 km^3 volume
Heidarzadeh et al. (2020a)	No collapse/slide modeling. Empirical initialization based on laboratory experiments	COMCOT: 2D nonlinear and non-dispersive long wave model (NLSW)	Single 8 arc-sec (250 m) resolution grid Bathy/topo: from GEBCO-2014 30 arc-sec (900 m) resolution data	0.005 to 0.677 km^3 volume (empirical). Best fit with observations: 0.175 km^3 volume
Borrero et al. (2020)	No collapse/slide modeling. initialization with analytical solution	pCOULWAVE: 2D fully nonlinear and dispersive Boussinesq model	Single 2 arc-sec (60 m) resolution grid Bathy/topo: not defined	Analytical source parameters adjusted to best match the near-field runups
Omira and Ramalho, (2020)	2D Viscoplastic/ Bingham slide model with upper water layer solving Nonlinear Shallow Water Eqs.	Same NSW model as slide model used for tsunami propagation.	Grid resolution not specified, Bathy/topo: DEMNAS 10 m topography and BIG 5 m bathymetry. A 10 m DEM is interpolated from both.	Two-failure sequence at 5 s, with 0.135 km^3 total volume, geometry reconstructed from pre-/post-collapse satellite observations
Dogan et al. (2021)	2D two-layer water/slide coupled model with dense fluid slide rheology	NAMI DANCE: 2D nonlinear and non-dispersive long wave model (NLSW)	Single 80 m resolution Cartesian grid Bathy/topo: from BATNAS 90-140 m resolution data	Reconstructed from pre-/post-collapse satellite observations with 0.24 km^3 volume (little detail given on definition of failure/slide geometry)

Table 1. Overview of main characteristics of earlier studies of the 2018 AK collapse and tsunami modeling.

Grid	Mesh size (*N, M*)	Resolution (m)	SW Corner (Lat., Lon.)
G1	3680,3900	50	-7°, 104.4°
G2	955, 1155	30 (horiz.) 7 σ (vert.)	-6.2357°, 105.2916°

1197 **Table 2:** Parameters of grids used in simulations with NHWAVE (G2) and FUNWAVE (G1) (Fig. 1).

WG	Lon E. (Deg.)	Lat N. (Deg.)	Depth (m)	*t* meas. crest (s)	*t* meas. 1 cm (s)	*t* sim. crest (s)	*t* sim. 1 cm (s)
1.	105.4066^o	-6.1234^o	239.50	N/A	N/A	53-65	15.6-24.2
2.	105.3733^o	-6.1524^o	88.22	N/A	N/A	165.1-175.5	118.0-127.0
3.	105.4246^o	-6.0691^o	49.32	N/A	N/A	179-191	131.2-140.0
4.	105.4954^o	-6.1279^o	58.50	N/A	N/A	244.5-254.5	197.5-208.0
5.	105.3571^o	-6.1361^o	90.74	N/A	N/A	188.5-190.4	165.5-169.4
6.	105° 50' 15.0"	-6° 11' 21.5"	4.70	1980	1923	1995-2006	1967-1979
7.	105° 57' 10.8"	-6° 01' 02.5"	3.64	2700	2587	2712-2727	2617-2629
8.	104° 37' 08.5"	-5° 30' 01.2"	3.67	2520	2292	2550-2568	2358-2382
9.	105° 19' 06.1"	-5° 28' 08.7"	3.92	3600	3390	3660-3678	3564-3624

1198

1199 **Table 3**: Parameters of numerical wave gauges (WG) 1-9 (Figs. 1a,b): Lat-Lon, depth (in grids G1

1200 (6-9) and G2 (1-5), assuming a MWL = MSL + 1.5 m, corresponding to the estimated average tide

1201 elevation at the time of the event), and arrival time (1 cm elevation or first main crest),

1202 measured/simulated range for 8 scenarios (Figs. 6,7; scenarios 1-8 in Table 4). WG 1-5 have no

1203 measured time (Fig. 6), but WG 6-9 are collocated with Tide Gauges (Fig. 10) at: (5) Serang,

1204 Marina Jambu, (6) Ciwandan, (8) Kota-Angung, (9) Panjang. In simulations, the AK collapse is

1205 assumed to take place at 20:57' local time (UTC + 7). Simulated crest arrival times at 9 WG for 8

1206 scenarios are within 2-18 s. Simulated differences in crest arrival time at tide gauges are 15-78 s,

1207 compared to the 1 minute data sampling interval. N/A: Not Applicable.

1208

1209

1210

No.	Landslide rheology	Collapse Volume. (km^3)	Model MWL (m)
1.	Granular	0.313	MSL + 1.5
2.	Granular	0.272	MSL + 1.5
3.	Granular	0.224	MSL + 1.5
4.	Granular	0.175	MSL + 1.5
5.	Viscous	0.313	MSL + 1.5
6.	Viscous	0.272	MSL + 1.5
7.	Viscous	0.224	MSL + 1.5
8.	Viscous	0.175	MSL + 1.5
9.	Granular	0.224	MSL + 0.5
10.	Granular	0.224	MSL + 1.0
11.	Granular	0.224	MSL + 2.0

1211

1212 **Table 4:** Description of Anak's collapse scenarios simulated in the near-field with NHWAVE, each for

1213 420 s (Figs 3-8; see Table 5 for rheology parameters). For each scenario, FUNWAVE is initialized with

1214 NHWAVE results at 380 s, and simulations are performed fin the far-field or an additional 2 h (Figs. 9,

1215 10); MSL and MWL denote the mean sea level and mean water level, respectively. Scenarios 1-8 are the

1216 main collapse scenarios simulated and discussed in the paper, whereas scenarios 9-11 are additional

1217 simulations performed as part of the sensitivity analysis of model results to MWL detailed in

1218 Supplementary file #S3. Scenarios 3, 7, 9-11 correspond to the likeliest collapse volume of 0.224 km^3.

1219 Scenario 3, with the granular rheology, is deemed our likeliest collapse scenario.

1220

Granular collapse rheology			
Granular medium density	ρ_c	1,900	kg/m^3
Granular bulk density	ρ_{ac}	1,550	kg/m^3
Internal friction angle	$\varnothing_{ic}$	10	°
Basal friction angle	$\varnothing_{bc}$	2	°
Viscous collapse rheology			
Viscous fluid density	ρ_c	1,550	kg/m^3
Viscous fluid kinematic viscosity	υ_c	0.5	m^2/s

1221 **Table 5:** Parameters of granular landslide and viscous landslide collapse scenarios simulated with

1222 NHWAVE (see Table 4).

1223

(a)

1224
1225

(b)

(c)
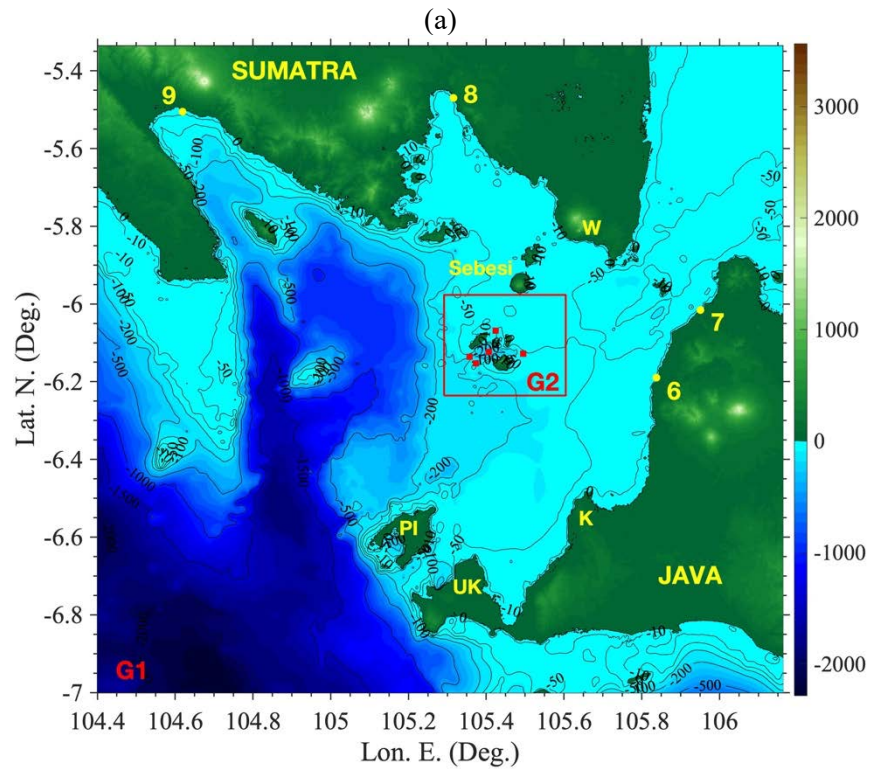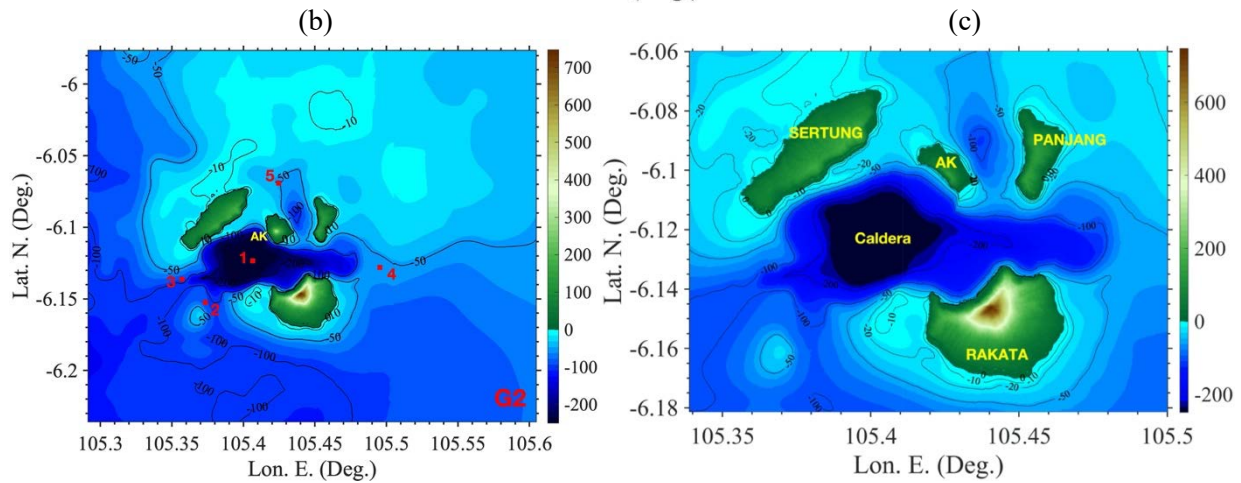
Figure 1: (a) Study area covered by 2D FUNWAVE 50 m Cartesian grid G1; (b) zoom-in onto 3D

NHWAVE 30 m Cartesian grid G2 (red box in (a)), with 7 vertical σ layers, encompassing Anak-

Krakatau (AK) and its surrounding islands (Rakata, Sertung, Panjang). Numbered symbols mark locations

of numerical wave gauges (6-9 are collocated with tide gauges). Black contours and color scale is (a,b)

pre- and (c) post-collapse (likeliest scenario) bathymetry/topography in meter, including an observed +1.5

m mean tide level. Letters in (a) are localities: (UK) Ujung Kulon; (K) Kolijaah; (PI) Panaitan Island; (W)

Waymuli.

56
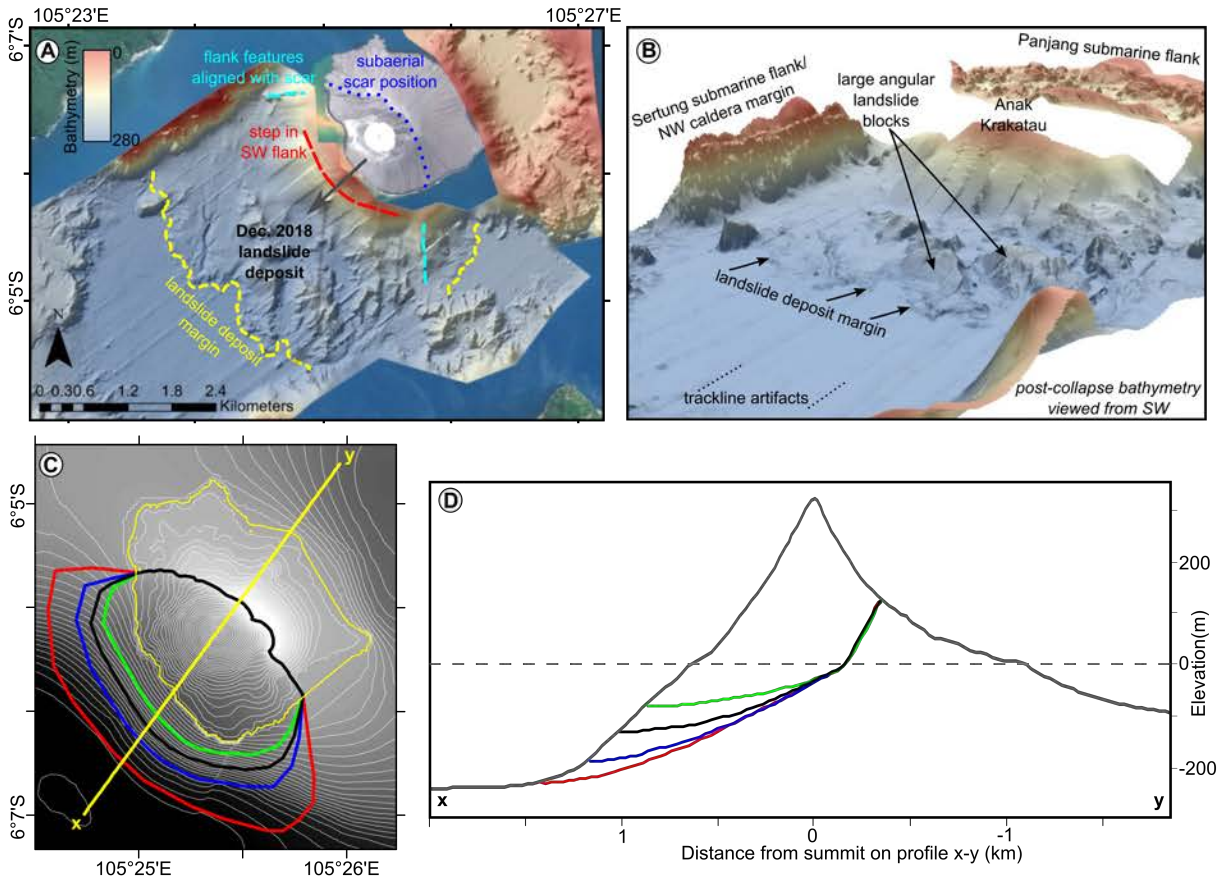
Figure 2: (a,b) Post-collapse bathymetry/topography of AK and surrounding islands (Fig 1) from August 2019 survey's seismic reflection profiles (Hunt et al., 2021), showing AK's subaerial scar and submarine landslide deposits; the rendering in panel (b) clearly shows large, blocky landslide deposits at the base of AK's SW flank. (c,d) Geometry of AK's four collapse scenarios modeled with NHWAVE, in (c) planview and (d) profile in SW direction (225 deg. to N; see trace in panel (c)), with colored lines marking the scenario of total collapse volume: (red) 0.313; (blue) 0.272; (black) 0.224 (deemed the likeliest volume scenario; see Figs. 1c and 3b and Table 4); and (green) 0.175 km^3. Yellow contour in (c) marks the post-collapse coastline and black line in (d) is AK's pre-collapse SW profile (culminating at 335 m).

1244

(a)

1245
1246

(b)
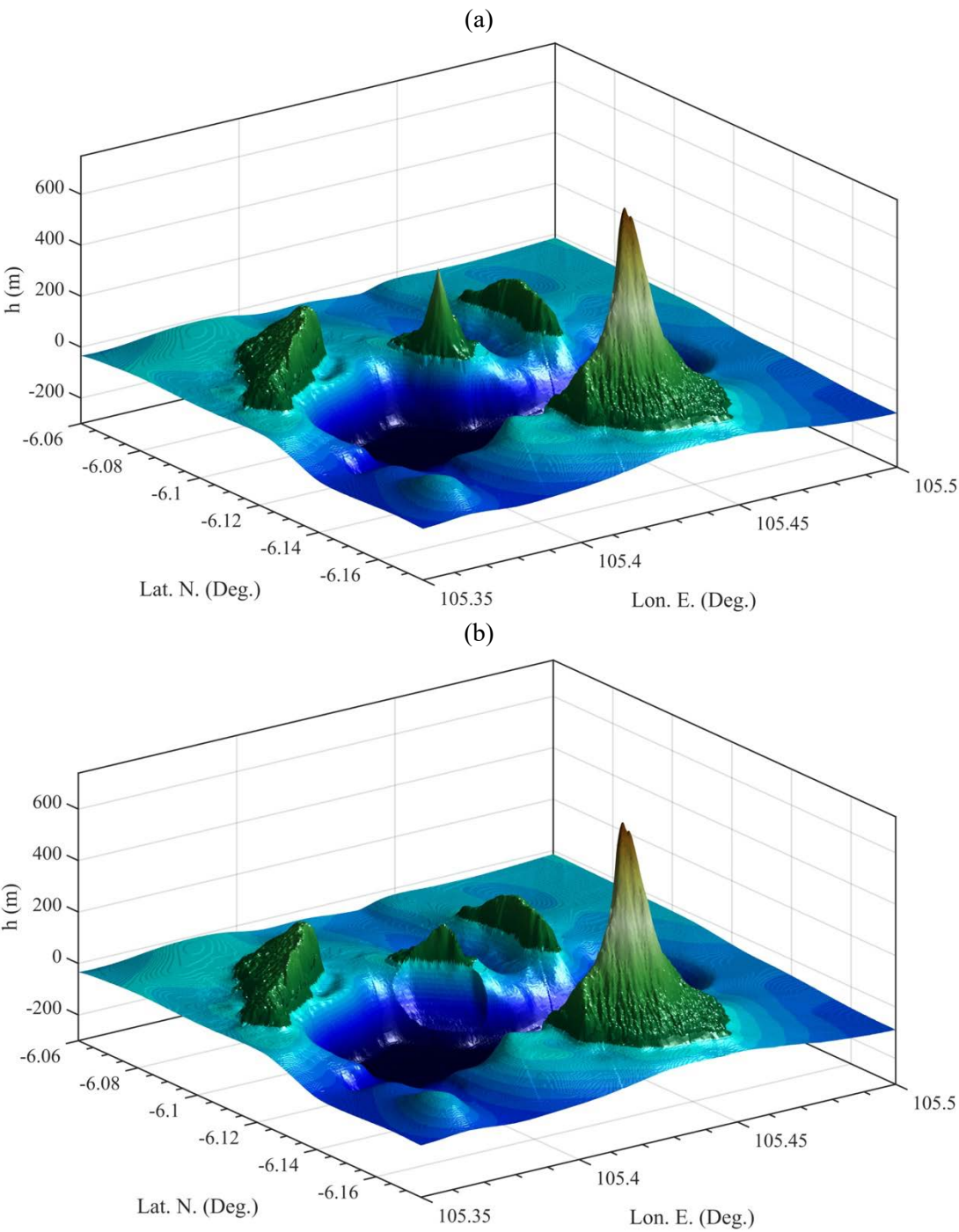
1247
1248   **Figure 3:** 3D view of composite pre- and post-collapse (likeliest scenario; #3 in Table 4)

1249   bathymetry/topography of AK and surrounding islands used in NHWAVE Grid G2 (Fig. 1c footprint),

1250   based on available pre-event data outside of Krakatau islands and August 2019 field survey data (see Fig.

1251   2) in the caldera and surrounding islands (Hunt et al., 2021). There is a factor 10 vertical exaggeration.

58

1252
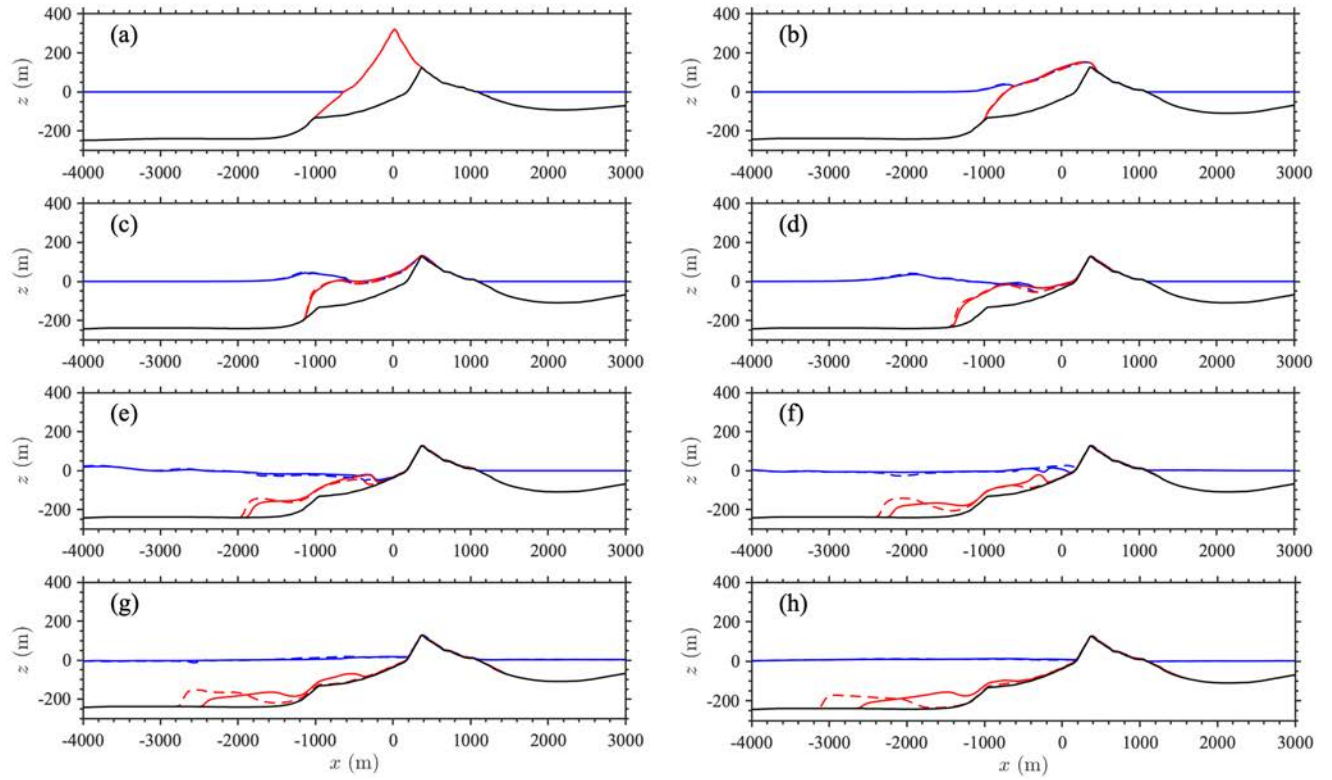
1253

Figure 4: Simulation of likeliest AK collapse volume scenarios (with 0.224 km^3; #3 and 7 in

Table 4) with NHWAVE in Grid G2 (Fig. 1) with a granular (solid; #3) or viscous (dashed; #7)

rheology. Sub-panels show SW (225 deg. to north; Fig. 2) transects of computed instantaneous

surface elevations (—/- - -) and slide profiles (—/- - -), at t = (a) 0, (b) 10, (c) 20, (d) 40, (e) 80,

(f) 120, (g) 160 and (h) 200 s.

1259

1260   (a)

1261   (b)

1262   (c)

1263   (d)
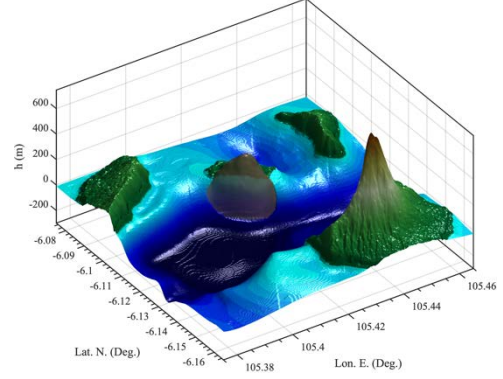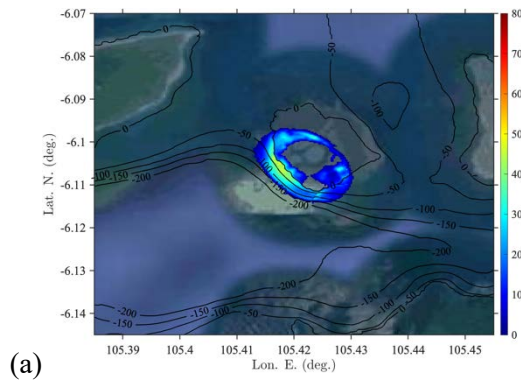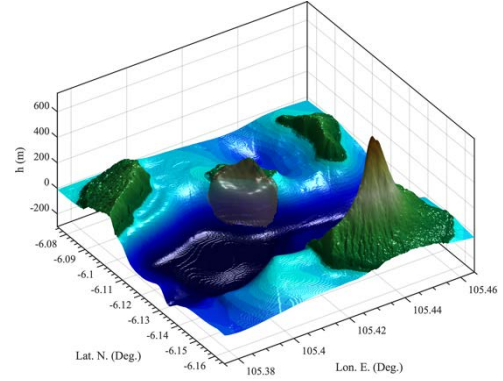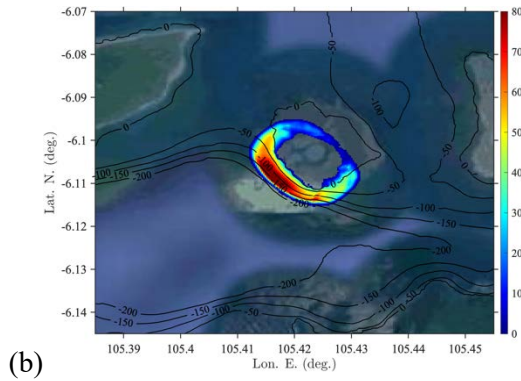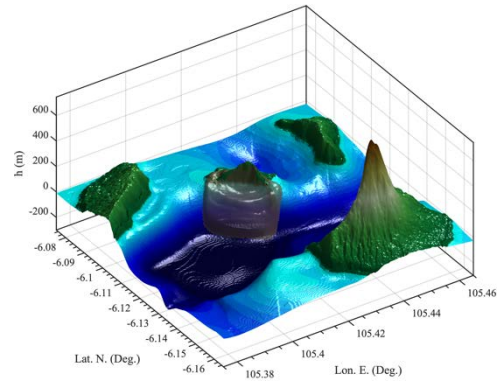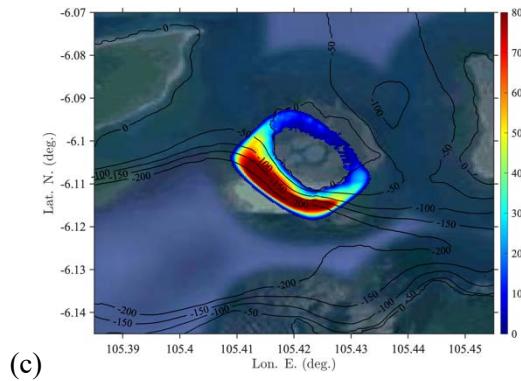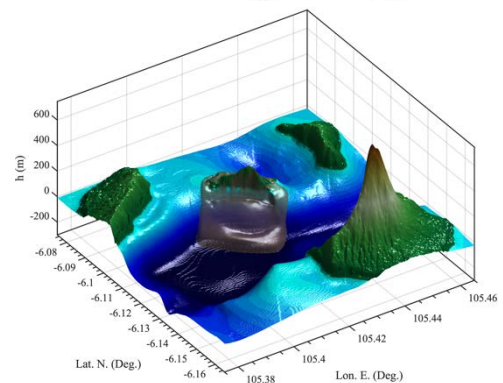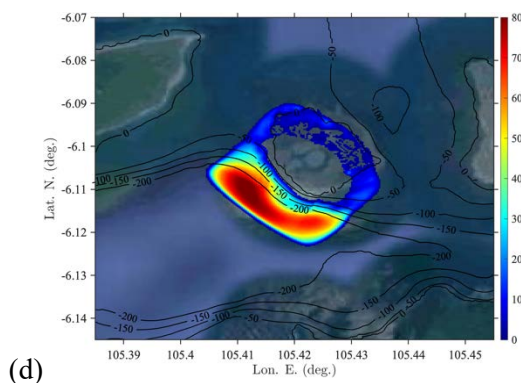
1264   **Figure 5:** Snapshots of slide motion for granular case of Fig. 4 (#3 in Table 4), at t = (a) 10, (b)

1265   20, (c) 40, (d) 80, (e) 120, (f) 160, (g) 200, and (h) 380 s. Color scale is slide thickness in meter.

1266   Contours are depth in meter.

1267

(e)

1268

(f)

1269

(g)
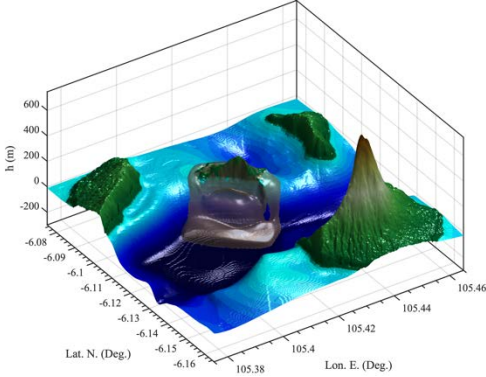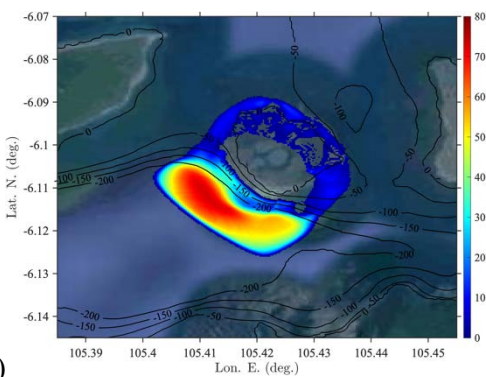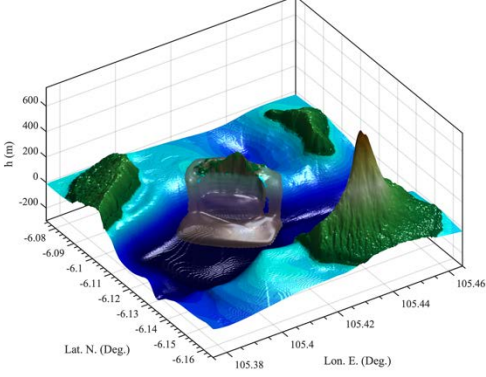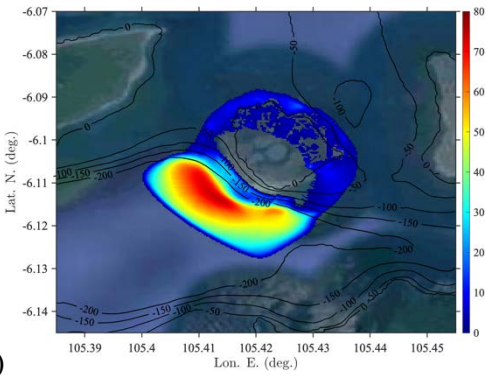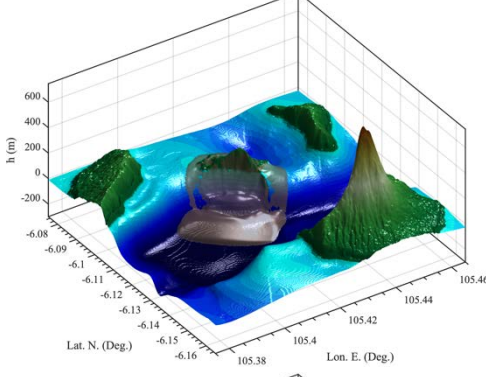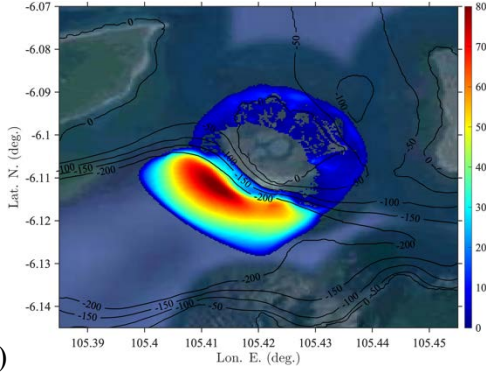
1270
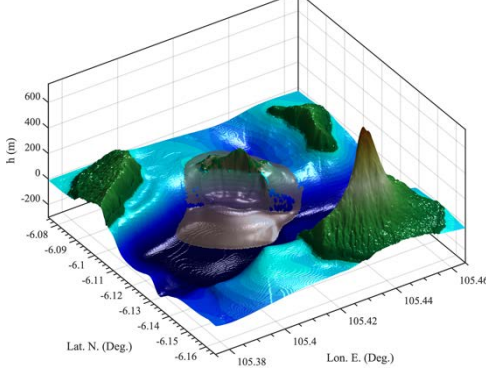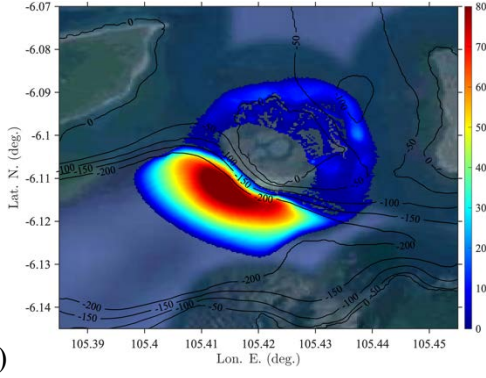
(h)

1271
1272
1273

Figure 5: continued.

1274

(a)

1275
1276

(b)

1277
1278

(c)

1279
1280

(d)

1281
1282

(e)
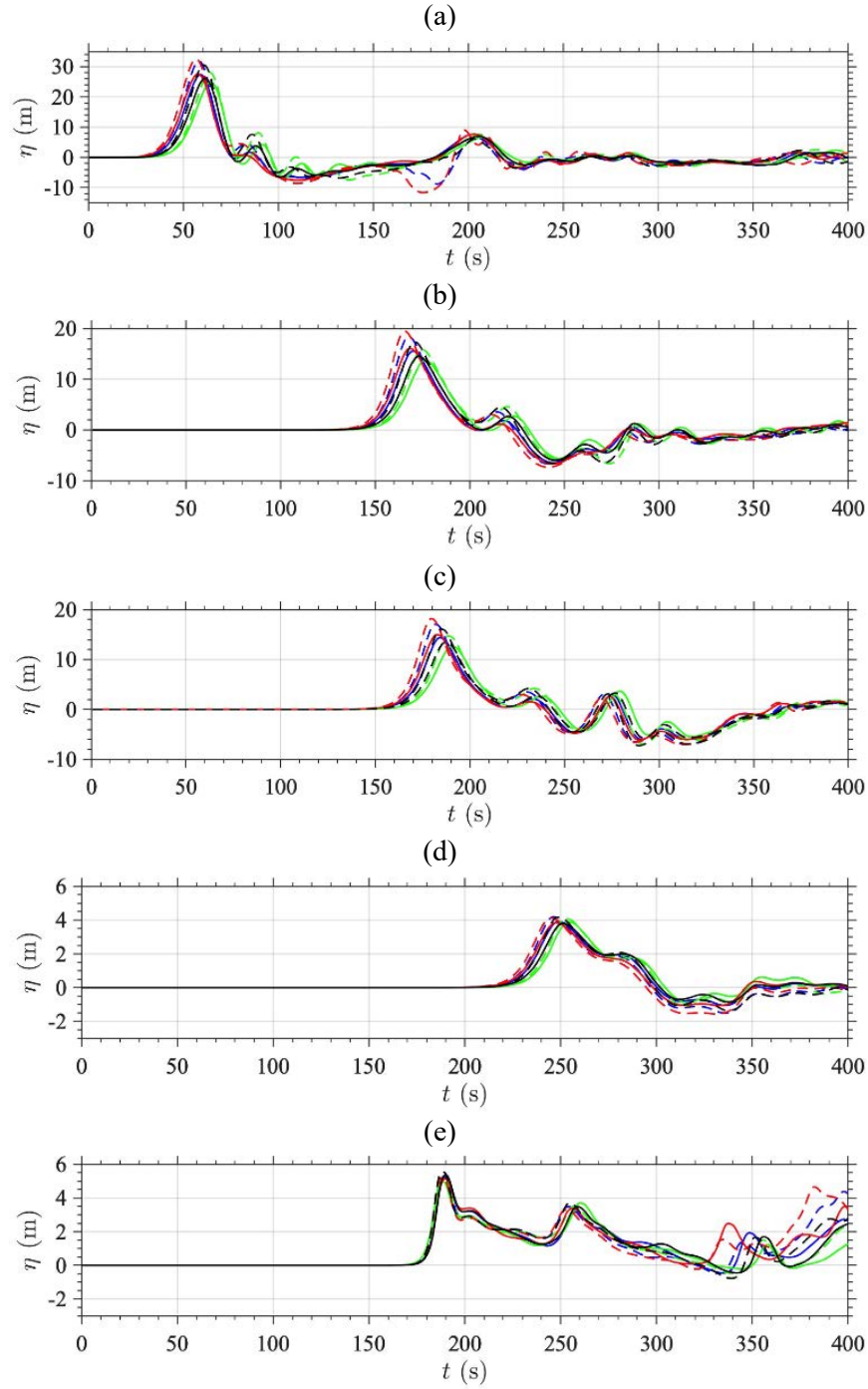
1283
1284   **Figure 6:** Time series of surface elevations computed at numerical wave gauges (WG) 1-5 (a-e; Fig. 1b)

1285   with NHWAVE in Grid G2 (Fig. 1), for 8 AK collapse scenarios (#1-8 in Table 4), with a granular

1286   (solid) or viscous (dashed) rheology, and volume (Figs. 2c,d): (—/- - -) 0.313; (—/- - -) 0.272; (—/- - -)

1287   0.224 (likeliest scenario; see Figs. 1c and 3b); (—/- - -) 0.175 km^3. Time $t = 0$ is estimated collapse time,

1288   20:57′ local time (UTC + 7). Note, reference level in <u>simulations</u> is MWL = MSL + 1.5 m (tide
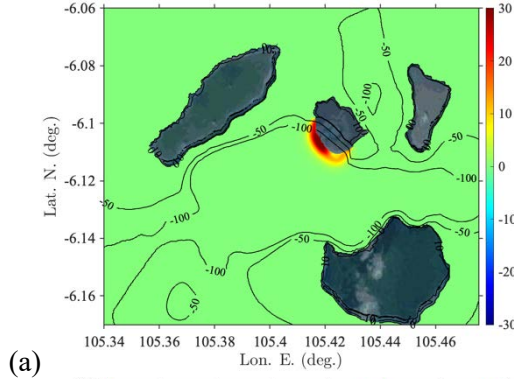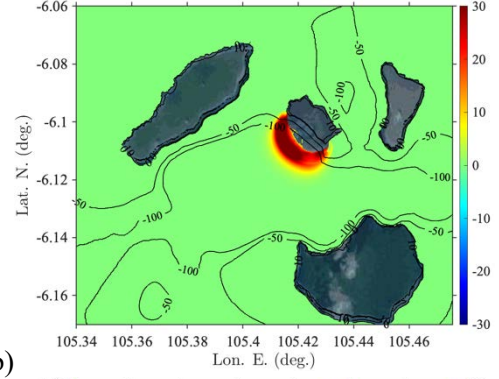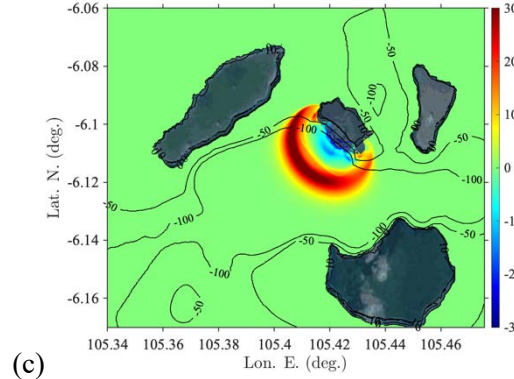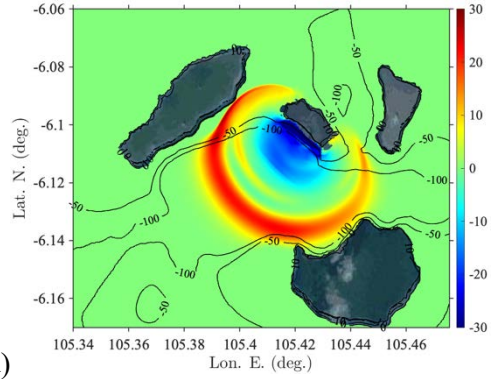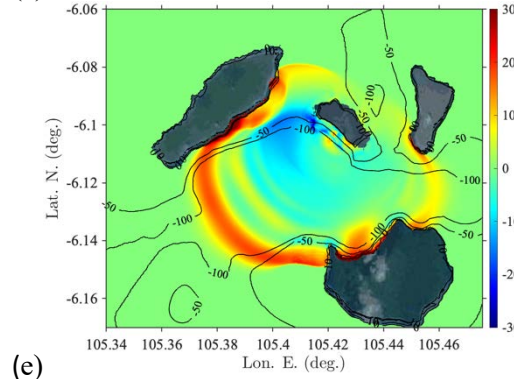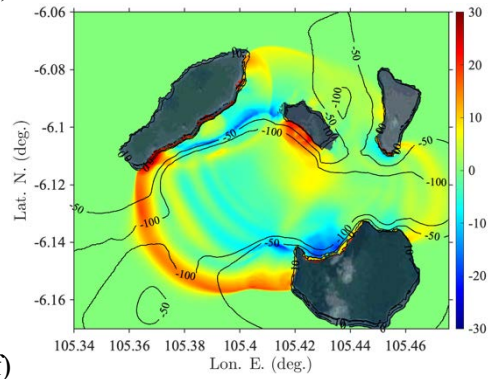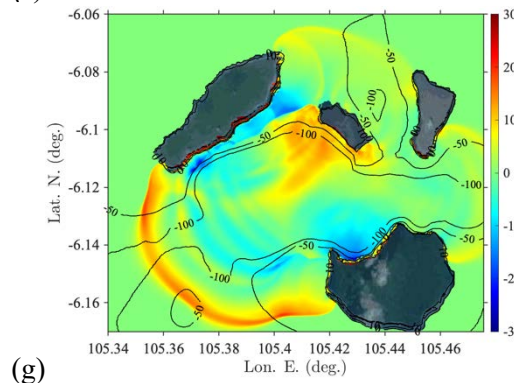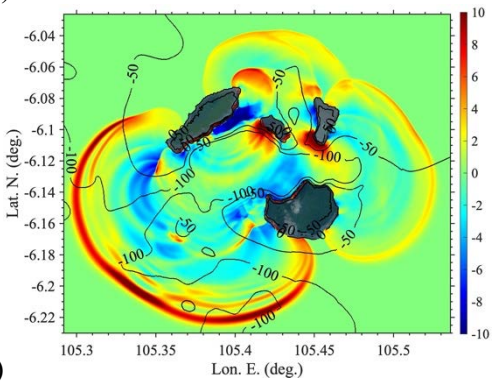
1289   elevation).

Figure 7: Snapshots of free surface elevations computed with NHWAVE in Grid G2, for likeliest collapse scenario (granular, 0.224 km^3; #3 in Table 4), at t = (a) 10, (b) 20, (c) 40, (d) 80, (e) 120, (f)160, (g) 200, and (h) 380 s (latter time is FUNWAVE initialization). Same case as Fig. 5. Reference level in simulations is MSL + 1.5 m.
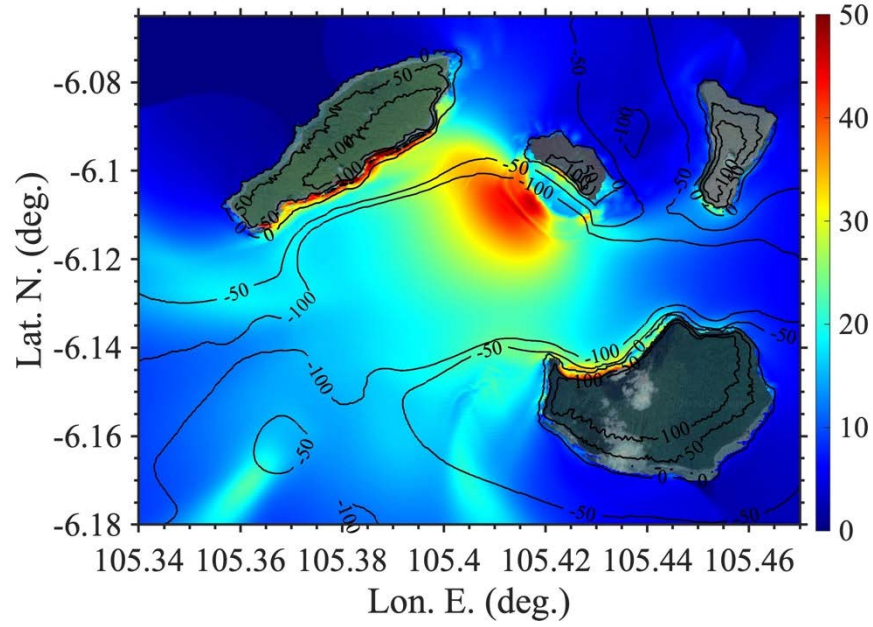
1298

1299

1300   **Figure 8:** Maximum envelope of surface elevations computed with NHWAVE in Grid G2 for AK

1301   collapse likeliest scenario (granular, 0.224 km^3; #3 in Table 4), up to $t = 420$ s (color scale in meter).

1302   Reference level in simulations is MWL = MSL + 1.5 m.

1303
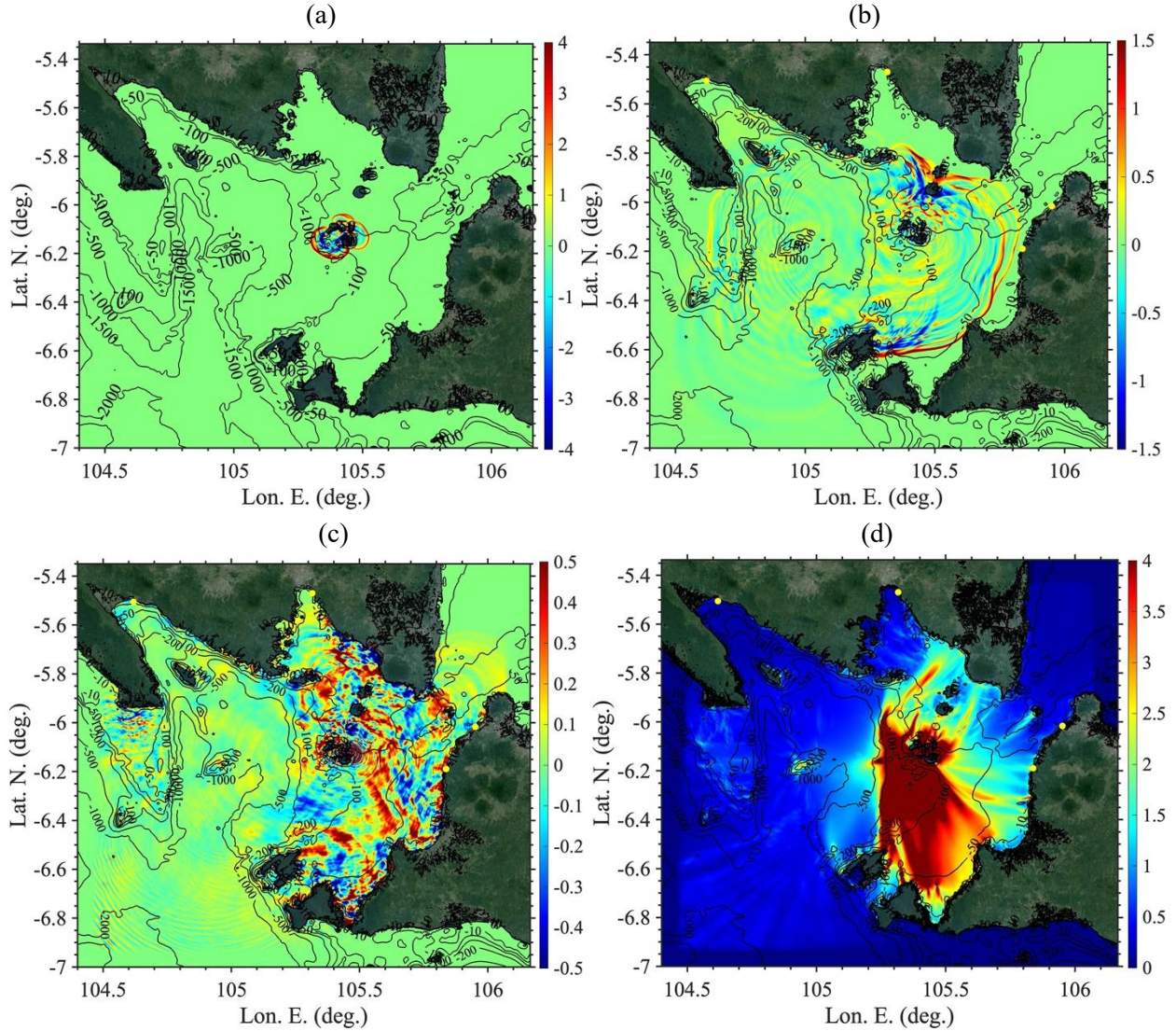
Figure 9: Tsunami surface elevations computed with FUNWAVE in Grid G1 for AK collapse likeliest scenario (granular, 0.224 km³; #3 in Table 4). Initial elevation at t = (a) 380 s from NHWAVE simulation, (b) 1800 s, and (c) 3600 s; (d) envelope of maximum elevations up to t = 7,580 s (different color scales in meter). Maps show topography from Google Earth georeferenced satellite images embedded using an API key. Reference level in simulations is MWL = MSL + 1.5 m. Yellow bullets mark locations of tide gauges (see Fig. 1a).

1317

(a)

1318
1319

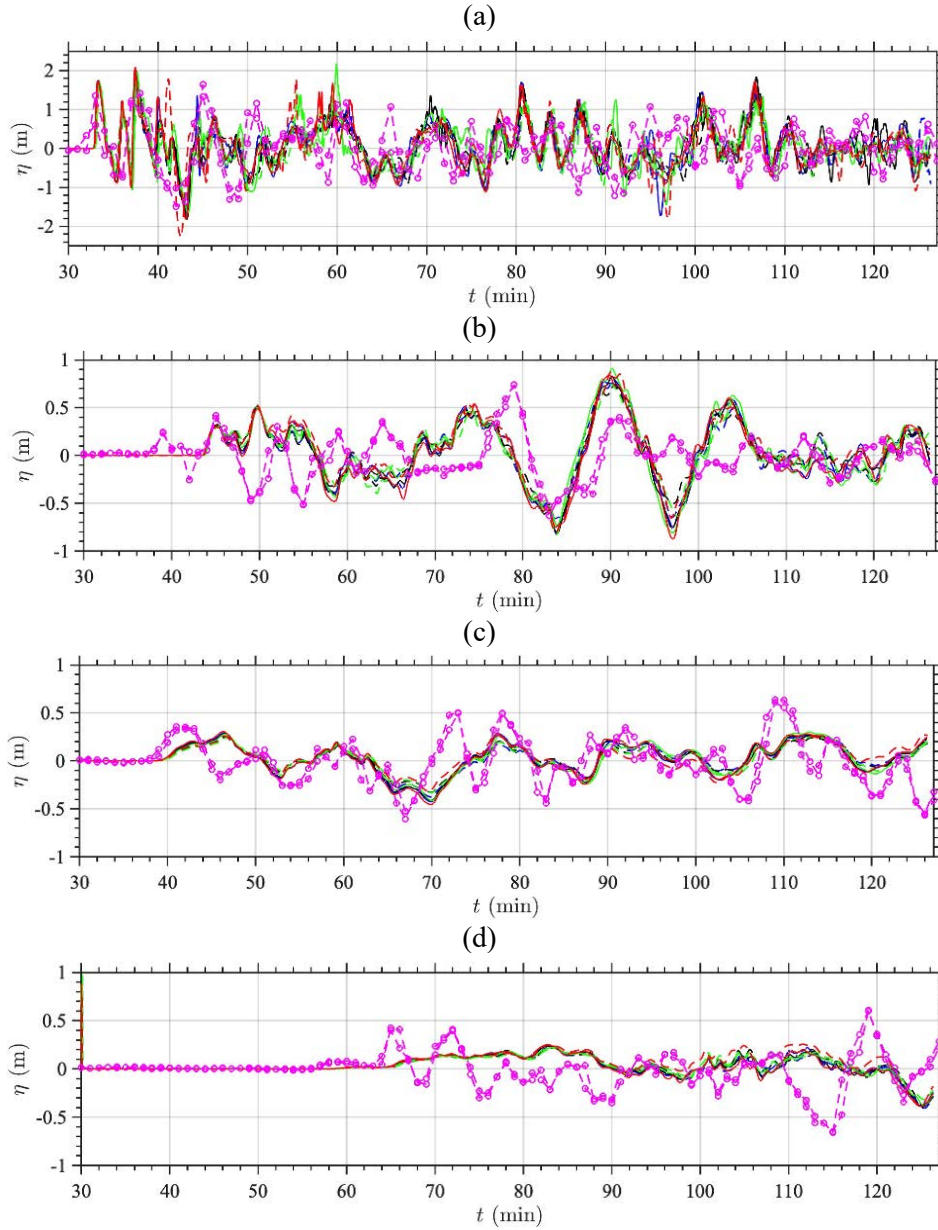(b)

1320
1321

(c)

1322
1323

(d)

1324

1325   **Figure 10:** Time series of surface elevations, in simulations with respect to MWL = MSL + 1.5 m, at

1326   numerical wave gauges 6-9 (a-d; Fig. 1a), computed with FUNWAVE for 8 AK collapse scenarios (#1-8

1327   in Table 4) with a granular (solid) or viscous (dashed) rheology, and volume (Figs. 2c,d): (——/- - -) 0.313;

1328   (——/- - -) 0.272; (——/- - -) 0.224 (likeliest scenario; see Figs. 1c and 3b); (——/- - -) 0.175 km^3, compared

1329   to collocated detided observations (-o-) with 2 sensors, at 4 tide gauges (Table 3). Time t = 0 is estimated

1330   collapse time, 20:57′ local time (UTC + 7).

1331

(a) (b)
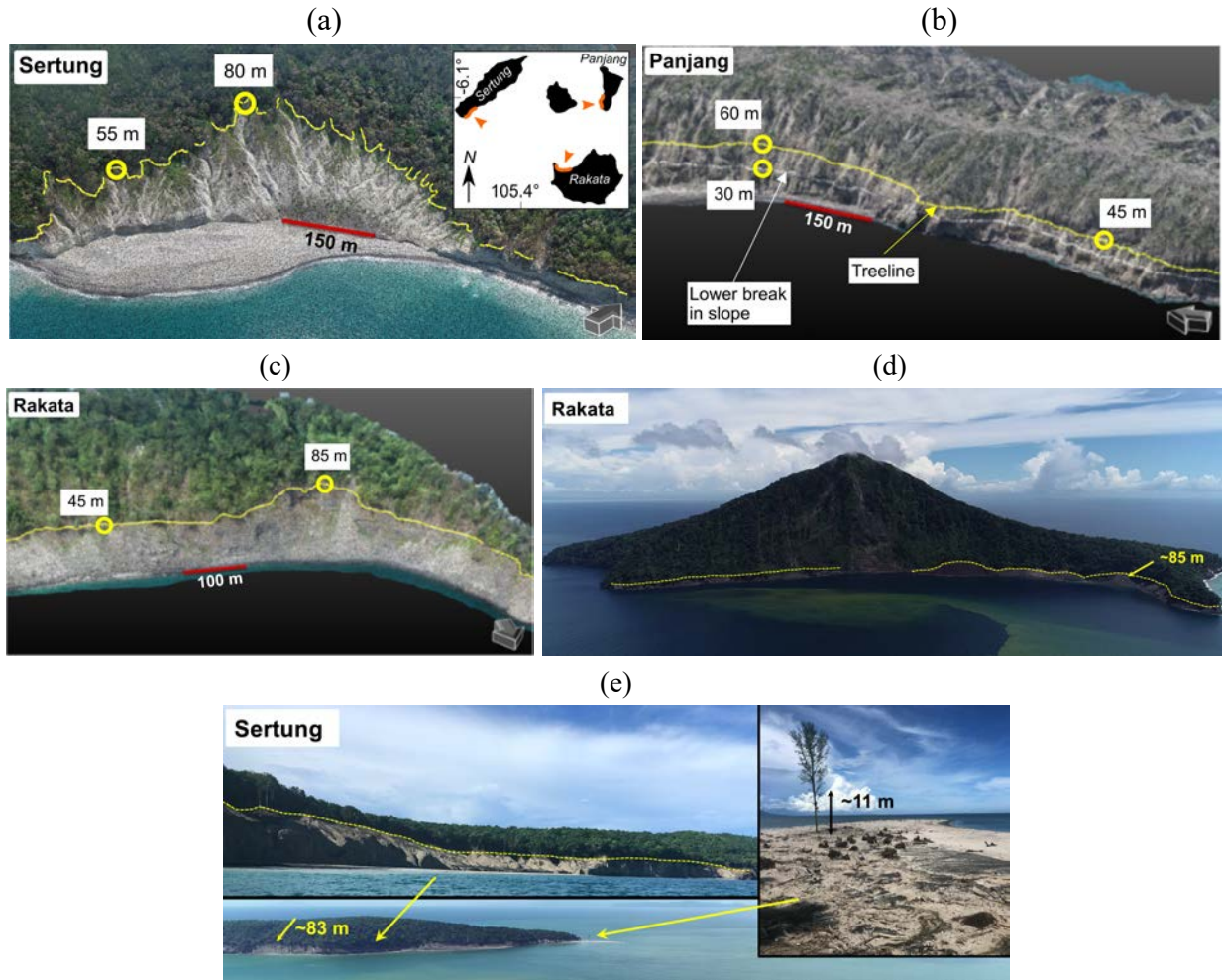

1333
1334 (c) (d)

1335
1336 (e)

1337

Figure 11: Pictures from AK field surveys of near-field runups (see Fig. 13 for actual elevations) on surrounding islands (Fig. 1c): (a,b,c) dashed yellow lines mark the authors August 2019 tree/vegetation line drone survey of Sertung, Panjang and Rakata, respectively (see inset in (a) for orientation); (d,e) Borrero et al.'s (2020) 02/2019 survey, of (d) Rakata's N/NW shore, (e) Sertung's SE/NE shore. In panel (b), the white dashed line marks the steepest slope limit on Panjang's W shore.
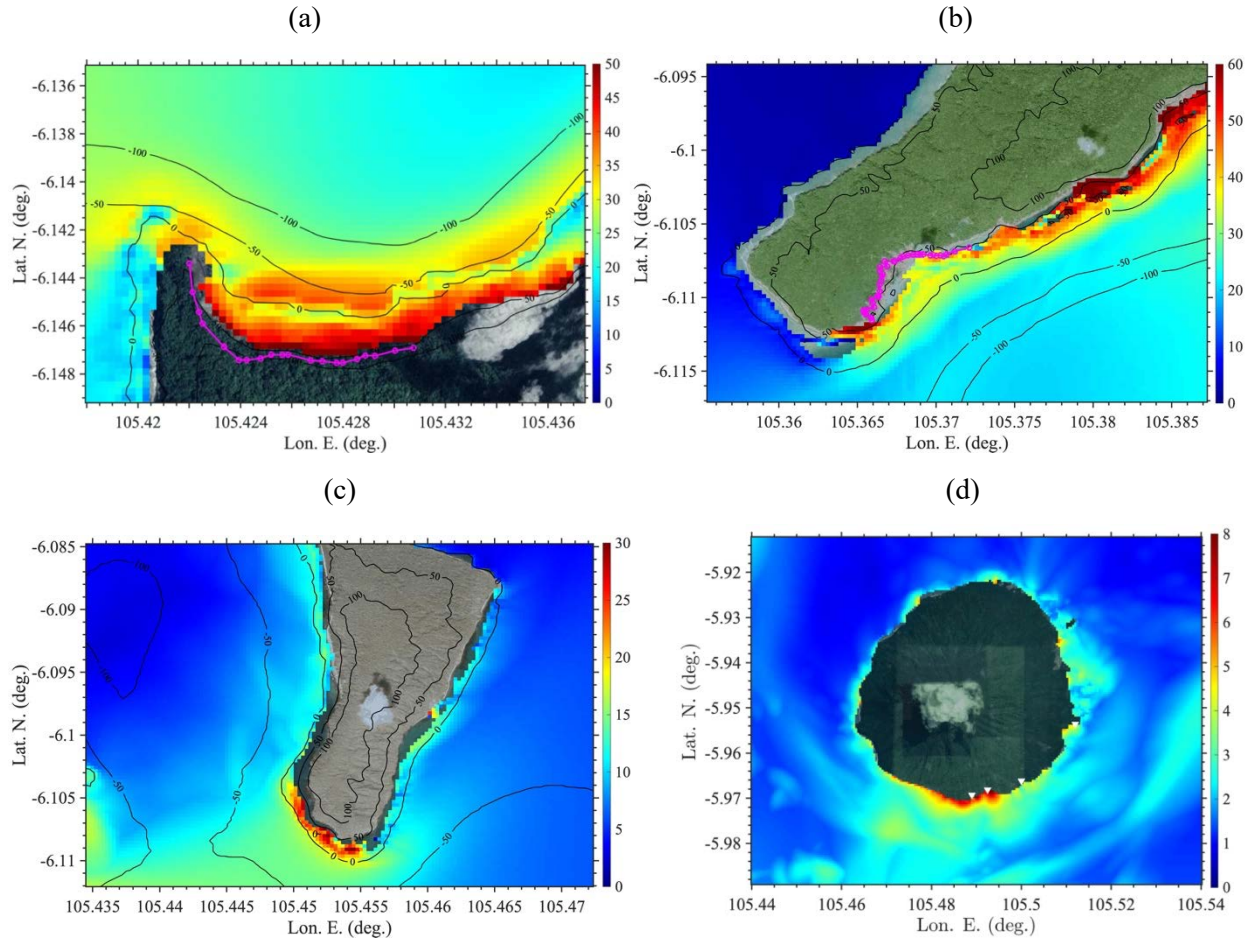
1343
1344

1345

67

1346   (a)   (b)

1347

1348   (c)   (d)

1349

1350

1351 **Figure 12:** Zoom-in on maximum surface elevation (inundation) computed with (a-c) NHWAVE in Grid

1352   G2 (Fig. 8) or (d) FUNWAVE in Grid G1 (Fig. 9d) for the likeliest collapse scenario (granular, 0.224

1353   km^3; #3 in Table 4), along (Figs. 1a,c): (a) Rakata's NW shore, (b) Sertung's SW shore, (c) Panjang's S

1354   shore, and (d) Sebesi. Pink circles/line in (a,b) indicate August 2019 drone survey (Figs. 11a,c); white

1355 triangles in (d) are flow depth/runup from Borrero et al.'s (2020) 02/2019 field survey of Sebesi (7.5, 9.0,

1356 2.6, 2.0 m from W to E, respectively, referred here to MWL). Black contours are bathymetry/topography

1357   in meter. Note, reference level in simulations is MWL = MSL + 1.5 m (tide elevation).
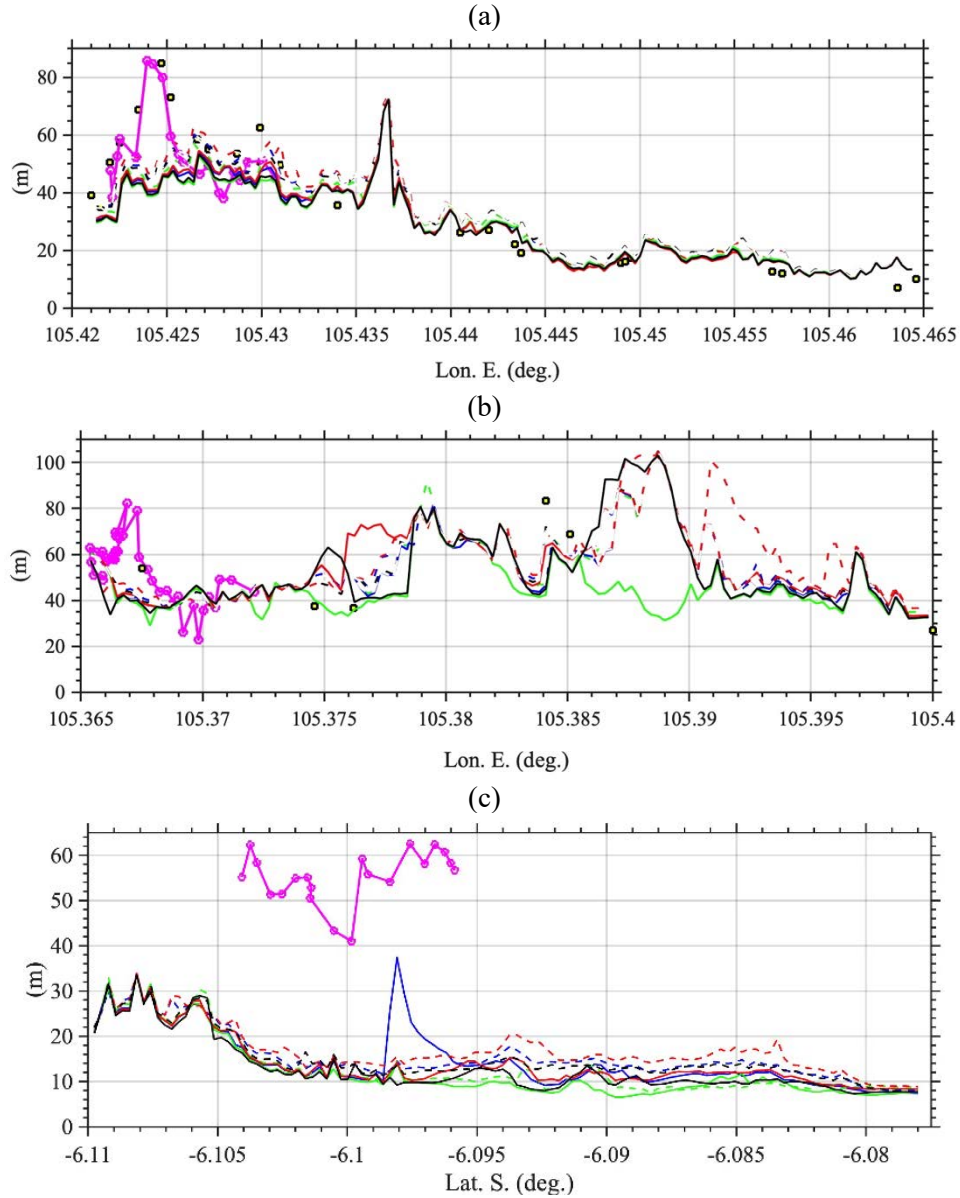
1358

1359

1360

(a)

(b)

(c)

Figure 13: Maximum runup computed with NHWAVE along (Figs. 1c, 11, 12): (a) Rakata's N shore; (b) Sertung's S shore; and (c) Panjang's W shore, for 8 AK collapse scenarios (#1-8 in Table 4) with a granular (solid) or viscous (dashed) rheology, and volume (Figs. 2c,d): (——/- - -) 0.313; (——/- - -) 0.272; (——/- - -) 0.224 (likeliest scenario; see Figs. 1c and 3b); (——/- - -) 0.175 km^3, compared to the authors' August 2019 drone field survey (Fig. 11; -o-) of tree line and to the field measurements (yellowed squares) of Borrero et al. (2020); note, the latter authors reported an 8 m flow depth for north of Panjang. Note, in simulations and the field data, zero elevation is MWL = MSL + 1.5 m (tide elevation).
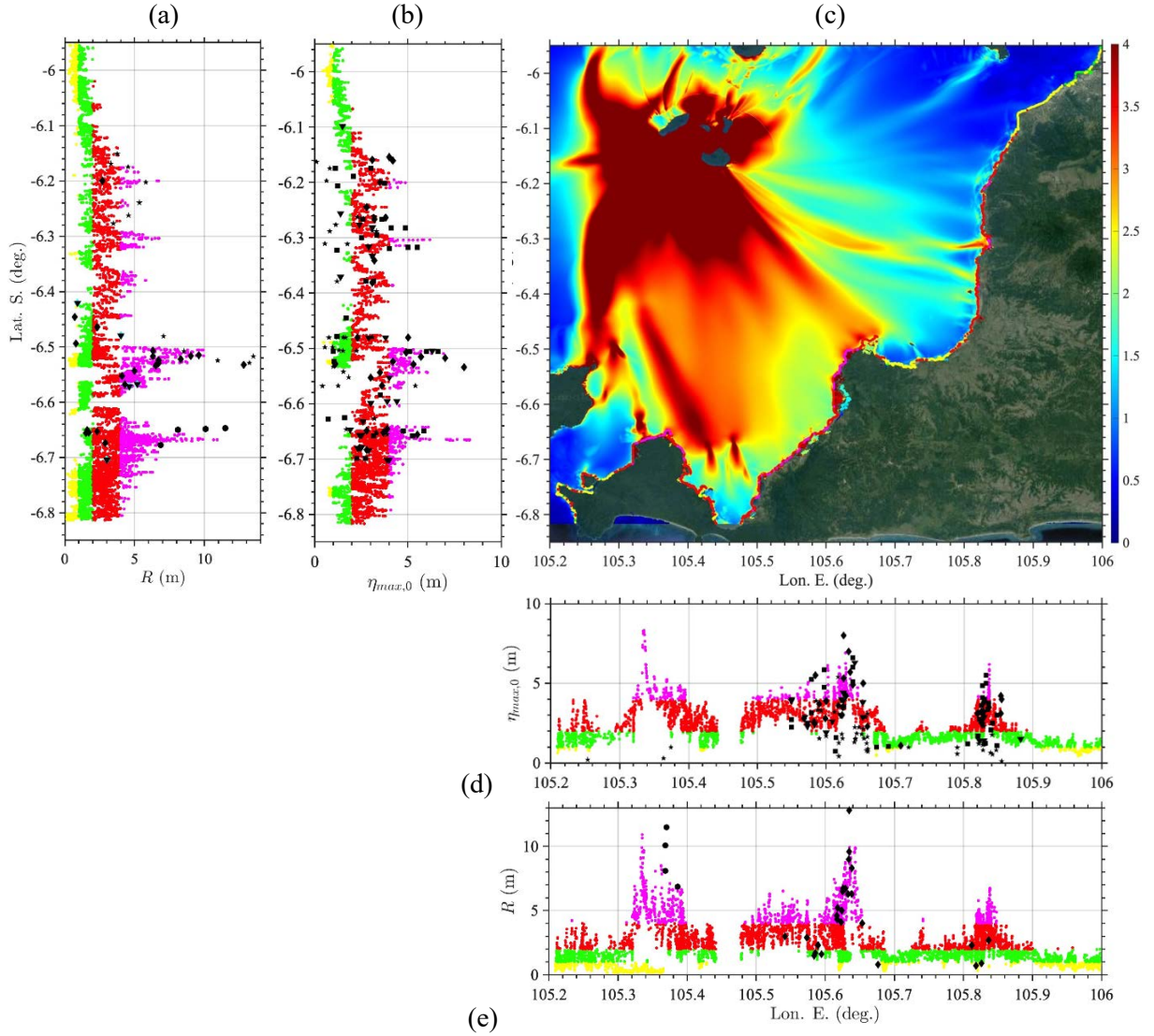
1376
1377

Figure 14: (a,e) Maximum Runup R, and (b,d) flow depth at the shore $\eta_{max,0}$ (along 0 m contour) from (a) maximum envelope of surface elevation computed with FUNWAVE in Grid G1, for likeliest AK collapse scenario (granular, 0.224 km^3; #3 in Table 4; Fig. 9d) zoomed-in on Java; for clarity, 4 classes of elevations are defined: (•) 0-1 m; (•) 1-2 m; (•) 2-4 m, and (•) > 4 m. Results are compared with field measurements of flow depth and runup, from: (■) TDMRC (2019), (★) Muhari et al. (2019), (◆) Putra et al. (2020), (▼) Heidarzadeh et al. (2020b), and (●) Borrero et al. (2020) surveys.
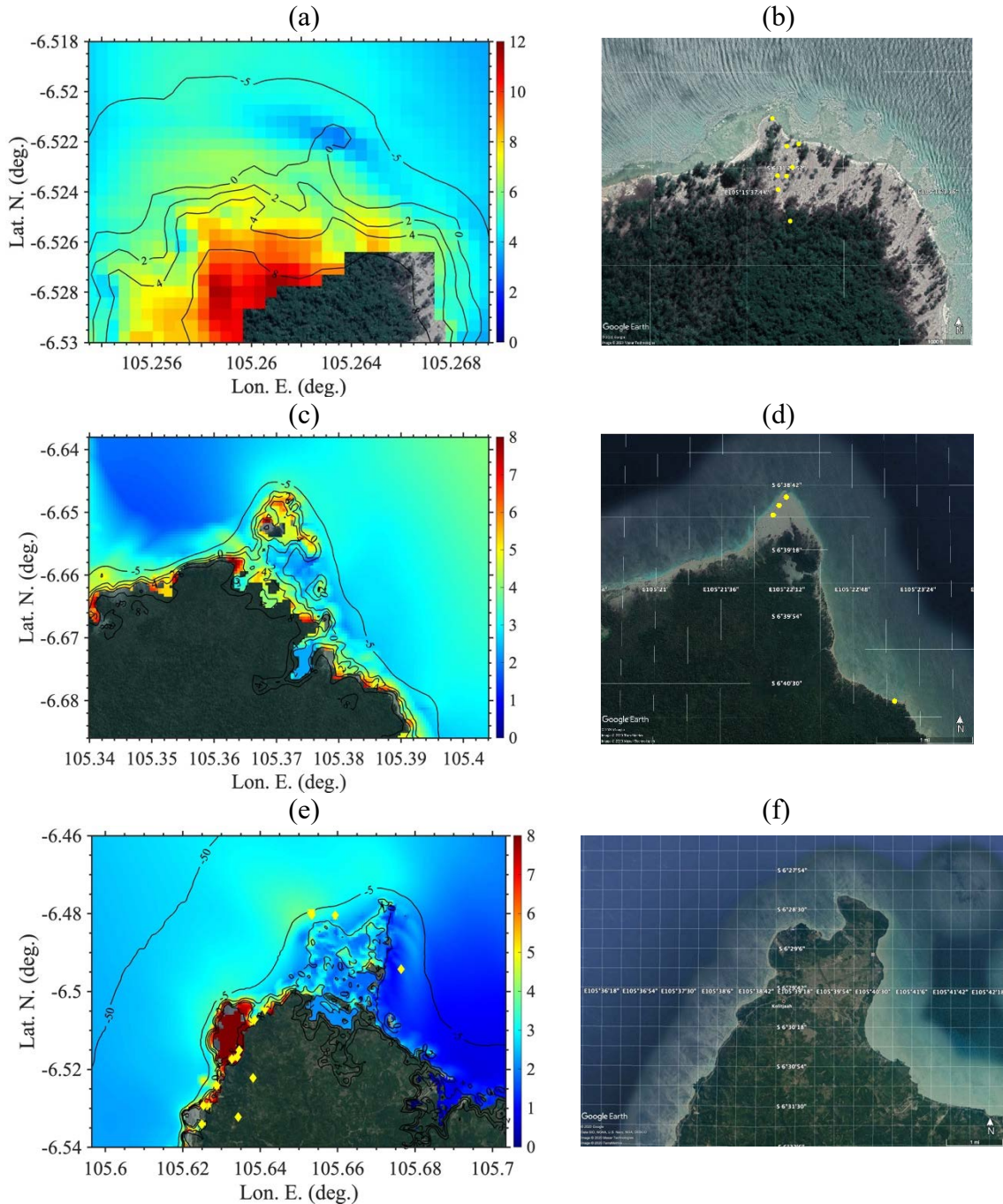
1388

Figure 15: (a,c,e) Max. surface elevation (FUNWAVE, Grid G1; color scales in meter), for likeliest AK collapse scenario (granular, 0.224 km^3; #3 in Table 4; Fig. 9d), zoomed on (Fig. 1a): (a) Panaitan Island (PI); (c) Ujung Kulon (UK); and (e) Kolijaah (K). (b,d,f) Google Earth image of PI, UK and K (11/20). (•) in (b,d) are locations of Borrero et al.'s (2020) elevation survey, measured from N to S, in (b) at (around Lon. E. 105.2622): 6.4, 7.3, 6.5, 6.1, 8.4, 6.4, 6, 7.4 m (MWL) (note southern point was missing a terrain correction that was added), and in (d) at: 11.5, 11.1, 8.1, 6.9 m (MWL). Black contours in (a,c,e) are bathymetry/topography in meter and color scale is maximum surface elevation in meter.
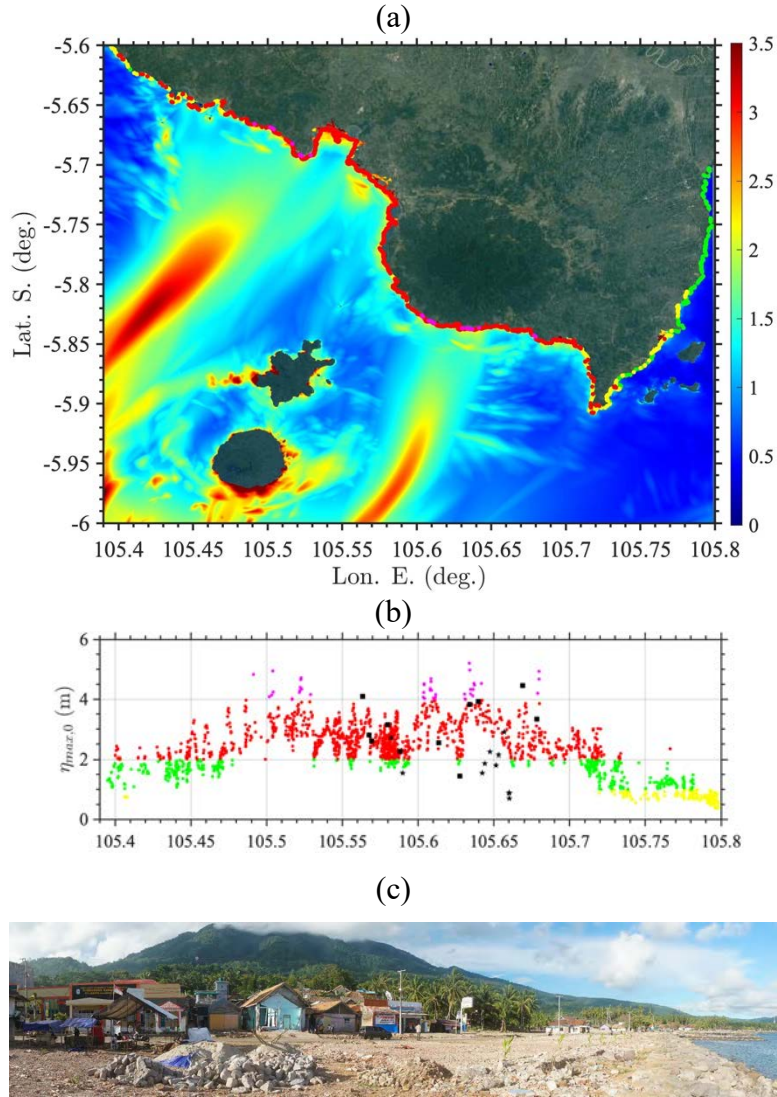
1402

(a)

1403
1404

(b)

1405
1406

(c)

1407
1408

1409   **Figure 16:** Same results as in Fig. 14: (a) Envelope of maximum surface elevation (FUNWAVE, Grid

1410   G1; color scales in meter), for likeliest AK collapse scenario (granular, 0.224 km^3; #3 in Table 4; Fig. 9d),

1411   zoomed on Sumatra (Fig. 1) with 4 classes defined as: (•) 0-1 m; (•) 1-2 m; (•) 2-4 m, and (•) > 4 m; (b)

1412   comparison of computed flow depth at the shore with field surveys of: (■) TDMRC (2019), (★) Muhari

1413   et al. (2019); (c) View of Waymuli (W, Fig. 1a, 105.6348 E), looking east, from Fritz et al. (2019)

1414   02/2019 field survey.